MNRAS 000, 1–16 (2016) Preprint 12 September 2016 Compiled using MNRAS LATEX style file v3.0

Modeling of deep gaps created by giant planets in protoplanetary discs

K.D. Kanagawa[1⋆], H. Tanaka[2], T. Muto[3], and T. Tanigawa[4]
[1] *Institute of Physics and CASA⋆, Faculty of Mathematics and Physics, University of Szezecin, Wielkopolska 15, PL-70-451 Szczecin, Poland*
[2] *Astronomical Institute, Tohoku University, Sendai, Miyagi 980-8578, Japan*
[3] *Division of Liberal Arts, Kogakuin University, 1-24-2 Nishi-Shinjuku, Shinjuku-ku, Tokyo 163-8677, Japan*
[4] *National Institute of Technology, Ichinoseki College, Ichinoseki-shi, Iwate 021-8511, Japan*

arXiv:1609.02706v1 [astro-ph.EP] 9 Sep 2016

Accepted XXX. Received YYY; in original form ZZZ

ABSTRACT

A giant planet embedded in a protoplanetary disc creates a gap. This process is important for both theory and observations. Gap openings are intimately connected with orbital migration and the mass growth of a planet. It has recently been observed that discs around young stars are rich in structure, and the interaction between a planet and a disc is considered to be one possible origin of this structure. We performed two-dimensional hydrodynamic simulations, varying the planet mass, disc aspect ratio, and viscosity in a wide range of parameters. This relationship enables us to judge whether an observed gap is likely to have been caused by an embedded planet. It is also possible to predict the planet mass from observations of the gap shape. Based on the results of hydrodynamic simulations, we present an empirical model of wave excitation and damping with deep gaps. Using this model of wave excitation and damping, we constructed a semianalytical model of the gap surface density distribution, and it reproduces the gap radial profile obtained from the two-dimensional hydrodynamic simulations.

Key words: accretion, accretion discs, protoplanetary discs, planets and satellites: formation, planet–disc interaction

1 INTRODUCTION

During the past decade, more than a thousand extrasolar planets have been discovered. A survey of extrasolar planets has revealed the diversity of giant planets outside the solar system (e.g., Burke et al. 2014). Giant planets are born in protoplanetary discs, due to core accretion (e.g., Mizuno 1980; Kanagawa & Fujimoto 2013) or to the gravitational instability of the gaseous disc (e.g., Cameron 1978; Zhu et al. 2012a). Once formed, they undergo orbital migration, and gas accretion results in growth their mass. The diversity of extrasolar planets is closely connected to such processes (e.g., Mordasini et al. 2012; Ida et al. 2013).

Planet forming regions in protoplanetary discs can now be directly imaged, such as by the Atacama Long Millimeter/Submillimeter Array (ALMA) and by eight-metre class optical and/or near-infrared telescopes. High-resolution images have revealed the presence of complex morphological structures in discs; these structures include spirals (e.g., Muto et al. 2012; Grady et al. 2013; Christiaens et al. 2014; Benisty et al. 2015; Currie et al. 2015; Akiyama et al. 2016) and gaps (e.g., Osorio et al. 2014; ALMA Partnership et al. 2015; Momose et al. 2015; Akiyama et al. 2015; Nomura et al. 2016; Yen et al. 2016; Tsukagoshi et al. 2016). Direct images are now finding possible signatures of planets being formed in discs (e.g., Sallum et al. 2015). To understand the origins of the disc structures and their possible connection to the formation of planets, it is important to construct appropriate quantitative models.

A planet interacts gravitationally with the gas in the surrounding disc, and as a result, the planet excites density waves (spirals). If the planet is sufficiently massive, it also creates gap structures (e.g., Lin & Papaloizou 1979; Goldreich & Tremaine 1980; Artymowicz & Lubow 1994; Kley 1999; Crida et al. 2006). Recently there have been a number of studies on the quantitative relationship between the mass of a planet and the gap structure (i.e., depth and width) (Duffell & MacFadyen 2013; Fung et al. 2014; Kanagawa et al. 2015b; Fung & Chiang 2016; Duffell & Chiang 2015; Kanagawa et al. 2016), and the application to actual observations has been discussed (Kanagawa et al. 2015b; Momose et al. 2015; van der Marel et al. 2016; Nomura et al. 2016;

⋆ E-mail:kazuhiro.kanagawa@usz.edu.pl

© 2016 The Authors

Tsukagoshi et al. 2016). However, there is still room for improvement of the current models. Kanagawa et al. (2016) presented an empirical formula for the gap width: they defined it to be the location at which the gap surface density is depleted by 50% from its original value. The overall structure of the gap created by the planet should be further investigated. Duffell (2015) constructed analytical models of the gap structure by using the wave damping model of Goodman & Rafikov (2001), which is particularly useful in the case of shallow gaps (created by relatively low-mass planets). Here, we note that the damping of spiral density waves excited by a planet (Takeuchi et al. 1996; Goodman & Rafikov 2001; Rafikov 2002; Dong et al. 2011) plays an important role in the exchange of angular momentum between the planet and the disc, and thus in forming the gap, as shown in the parametrized study by Kanagawa et al. (2015a) (hereafter, K15).

In this paper, we extend our previous model of the gap width and depth, and present a complete model of the gap shape; this is based on a number of two-dimensional long-term hydrodynamic simulations. In Section 2, we discuss the basic equations used in the two-dimensional simulations and present the numerical method and setting. In Section 3, we present our numerical results and obtain an empirical formula for the gap structure. In Section 4, we use our computational results to obtain a semianalytical model of the gap structure. In Section 5, we discuss the excitation and propagation of the density waves when a deep gap is formed. Section 6 contains a summary and discussion.

2 BASIC EQUATIONS AND NUMERICAL METHOD

2.1 Basic equations in a two-dimensional disc

We numerically computed the disc structures when a planet was present to investigate the gap formation induced by the planet. We assumed a geometrically thin and non-self-gravitating disc. We used a cylindrical coordinate system (R, ϕ, z), and the origin was located at the position of the central star. The velocity is denoted as $\boldsymbol{v} = (\mathrm{v_R}, \mathrm{v}_\phi, 0)$, where $\mathrm{v_R}$ and v_ϕ are the velocities in the radial and azimuthal directions. We assume that the vertical structure is in hydrostatic equilibrium. The angular velocity is denoted by $\Omega = \mathrm{v}_\phi/\mathrm{R}$. In this paper, we adopt a simple isothermal equation of state, in which a vertically integrated pressure P is given by $c^2\Sigma$, where c is the isothermal speed of sound, and Σ is the surface density, which is defined by $\Sigma = \int_{-\infty}^{\infty} \rho dz$, in which ρ is the gas density.

The vertically integrated equation of continuity is

$$\frac{\partial \Sigma}{\partial t} + \nabla \cdot (\Sigma \boldsymbol{v}) = 0. \tag{1}$$

The equations of motion in the radial and azimuthal directions are

$$\frac{\partial \mathrm{v_R}}{\partial t} + (\boldsymbol{v}\cdot\nabla)\,\mathrm{v_R} - \frac{\mathrm{v}_\phi^2}{\mathrm{R}} = -\frac{c^2}{\Sigma}\frac{\partial \Sigma}{\partial R} - \frac{\partial \Psi}{\partial R} + \frac{f_R}{\Sigma}, \tag{2}$$

$$\frac{\partial \mathrm{v}_\phi}{\partial t} + (\boldsymbol{v}\cdot\nabla)\,\mathrm{v}_\phi + \frac{\mathrm{v_R v}_\phi}{\mathrm{R}} = -\frac{c^2}{\Sigma R}\frac{\partial \Sigma}{\partial \phi} - \frac{1}{R}\frac{\partial \Psi}{\partial \phi} + \frac{f_\phi}{\Sigma}, \tag{3}$$

where f_R and f_ϕ are the viscous force per unit area acting in the R and ϕ directions:

$$f_R = \frac{2}{R}\frac{\partial}{\partial R}\left(\nu\Sigma R\left[\frac{\partial \mathrm{v_R}}{\partial R} - \frac{1}{3}\nabla\cdot\boldsymbol{v}\right]\right) + \frac{1}{R}\frac{\partial}{\partial \phi}\left(\nu\Sigma R\left[\frac{\partial \Omega}{\partial R} + \frac{1}{R^2}\frac{\partial \mathrm{v_R}}{\partial \phi}\right]\right), \tag{4}$$

$$f_\phi = \frac{2}{R}\frac{\partial}{\partial \phi}\left(\nu\Sigma\left[\frac{\partial \Omega}{\partial \phi} + \frac{\mathrm{v_R}}{R} - \frac{1}{3}\nabla\cdot\boldsymbol{v}\right]\right) + \frac{1}{R^2}\frac{\partial}{\partial R}\left(\nu\Sigma R^3\left[\frac{\partial \Omega}{\partial R} + \frac{1}{R^2}\frac{\partial \mathrm{v_R}}{\partial \phi}\right]\right). \tag{5}$$

The gravitational potential Ψ is given by

$$\Psi = -\frac{\mathrm{GM_p}}{\left[R^2 + 2RR_\mathrm{p}\cos(\phi-\phi_p) + R_\mathrm{p}^2 + \epsilon^2\right]^{1/2}} - \frac{\mathrm{GM}_*}{R} + \frac{\mathrm{GM_p}}{R_\mathrm{p}^2}R\cos(\phi-\phi_p), \tag{6}$$

where G is the gravitational constant, M_* is the mass of the central star, and M_p is the mass of the planet, which is located at (R_p,ϕ_p). The softening parameter is denoted by ϵ. The first and second terms in equation (6) are the gravitational potentials of the planet and the central star, respectively. The third term is an indirect term that reflects the fact that the coordinate system based on the central star is accelerated by the planet.

2.2 Numerical method

To numerically solve equations (1) to (3), we use the two-dimensional numerical hydrodynamic code FARGO[1], which is an Eulerian polar grid code with a staggered mesh. Because of a fast advection algorithm that removes the azimuthally averaged velocity for the Courant time step (Masset 2000), we can use FARGO to calculate the disc–planet interaction for a long period of time.

The gap is opened by the disc–planet interaction and is closed by the viscous diffusion. In steady state, the viscous angular momentum flux is balanced by the planetary torque. The timescale of the gap opening would be scaled by the viscous timescale (e.g., Lynden-Bell & Pringle 1974). As an empirical formula, the gap width, which is defined as a width of a region where the surface density is smaller than $0.5\Sigma_0$ in steady state, is obtained as follows (Kanagawa et al. 2016):

$$\frac{\Delta_\mathrm{gap}}{R_\mathrm{p}} = 0.41K'^{1/4}, \tag{7}$$

where

$$K' = \left(\frac{M_\mathrm{p}}{M_*}\right)^2\left(\frac{h_\mathrm{p}}{R_\mathrm{p}}\right)^{-3}\alpha^{-1}. \tag{8}$$

The timescale of the gap opening is

$$t_\mathrm{vis} = \left(\frac{\Delta_\mathrm{gap}}{2R_\mathrm{p}}\right)^2\left(\frac{h_\mathrm{p}}{R_\mathrm{p}}\right)^{-2}\alpha^{-1}\Omega_p^{-1}. \tag{9}$$

[1] See: http://fargo.in2p3.fr/

Using equation (7), this timescale is obtained as

$$t_{\rm vis} = 0.24 \left(\frac{M_{\rm p}/M_*}{10^{-3}}\right) \left(\frac{h_{\rm p}/R_{\rm p}}{0.05}\right)^{-7/2} \left(\frac{\alpha}{10^{-3}}\right)^{-3/2} \times \left(\frac{M_*}{1M_\odot}\right)^{-1/2} \left(\frac{R_{\rm p}}{10{\rm AU}}\right)^{3/2} {\rm Myr}. \quad (10)$$

To obtain the steady state, we have to calculate the evolution until $t \sim t_{\rm vis}$, as shown in the next section. Note that for nominal parameters, this timescale is usually shorter than or comparable with the migration timescale of the type II ($\sim R_p^2/\nu$) or disc lifetime ($\sim$ 1Myr). Hence, a full–width gap can be observed.

The computational domain runs from $R/R_{\rm p} = 0.4$ to $R/R_{\rm p} = 4.0$ with 1024×2048 radial and azimuthal zones. The resolution is about $h_{\rm p}/22$ in the radial direction and $h_{\rm p}/16$ in the azimuthal direction, where h is the scale height of the disc. The suffix p will be used below to indicate the value at $R = R_{\rm p}$. For simplicity, we neglect the disc gas accretion onto the planet and the planetary migration. The orbital radius of the planet is fixed at $R/R_{\rm p} = 1$. We adopt a constant kinematic viscosity coefficient ν, but we also use a viscous parameter α defined by α–prescription (Shakura & Sunyaev 1973), i.e., $\nu = \alpha ch$. The scale height is also set to be constant throughout the disc. We performed 34 hydrodynamic simulations with varying planetary masses, disc aspect ratios, and viscosities; the parameters adopted in our simulations are listed in Table 1. We also show an end time of each run in the table. We used the gravitational potential given by equation (6). The softening parameter ϵ in equation (6) was set to $0.6h_{\rm p}$.

Note that at the beginning of the simulation, we provide a turn-on phase for the planetary mass. During this phase, the planet's mass smoothly builds up from zero to the indicated value; this is done using the ramp function defined by $\sin^2[\pi t/(64{\rm P_{orbit}})]$. The mass reaches the indicated value after 32 orbital periods at that location.

The initial disc structures of the surface density, velocity, and temperature are axisymmetric against the location of the central star. The surface density is constant over the whole computational domain. The initial angular velocity is given as $\Omega_{\rm K}\sqrt{1-\eta}$, where $\Omega_{\rm K} = \sqrt{{\rm GM_*/R^3}}$ is the Keplerian angular velocity, and $\eta = (1/2)(h/R)^2 d\ln P/d\ln R$. The radial drift velocity is given by $v_R = -3\nu/(2R)$.

On the inner and outer boundaries ($R/R_{\rm p} = 0.4$ and $R/R_{\rm p} = 4.0$, respectively), the initial surface densities and velocities were maintained. In addition, to avoid artificial reflection of waves from the boundaries of the computational domain, we provided wave-killing zones near the boundary layers ($0.4 < R/R_{\rm p} < 0.5$ and $3.2 < R/R_{\rm p} < 4.0$) (cf., de Val-Borro et al. 2006). In the wave-killing zones, the surface density and radial and azimuthal velocities are related to their initial values as follows:

$$\frac{dX}{dt} = -\frac{X - X(t=0)}{\tau_{\rm damp}} f(R/R_{\rm p}), \quad (11)$$

where X represents Σ, $\rm v_R$, and $\rm v_\phi$; and $\tau_{\rm damp}$ is the orbital period at the boundary. The function f is a parabola of the form $y = x^2$, scaled to be zero at the boundary layer and unity at the opposite edge of the wave-killing zone.

Table 1. Model parameters

Run	M_p/M_*	$h_{\rm p}/R_{\rm p}$	α	End time (orbits)
1	5×10^{-4}	1/30	1×10^{-2}	1×10^{4}
2	1×10^{-3}	1/30	1×10^{-2}	1×10^{4}
3	5×10^{-4}	1/20	1×10^{-2}	1×10^{4}
4	1×10^{-3}	1/20	1×10^{-2}	1×10^{4}
5	5×10^{-4}	1/30	4×10^{-3}	1×10^{4}
6	1×10^{-3}	1/30	4×10^{-3}	1×10^{4}
7	1×10^{-4}	1/20	4×10^{-3}	1×10^{4}
8	5×10^{-4}	1/20	4×10^{-3}	1×10^{4}
9	1×10^{-3}	1/20	4×10^{-3}	1×10^{4}
10	1×10^{-3}	1/15	4×10^{-3}	1×10^{4}
11	2×10^{-3}	1/15	4×10^{-3}	1×10^{4}
12	2×10^{-3}	2/15	4×10^{-3}	1×10^{4}
13	5×10^{-4}	1/30	1×10^{-3}	2×10^{4}
14	1×10^{-3}	1/30	1×10^{-3}	2×10^{4}
15	5×10^{-5}	1/25	1×10^{-3}	1×10^{4}
16	1×10^{-4}	1/25	1×10^{-3}	1×10^{4}
17	5×10^{-4}	1/25	1×10^{-3}	1×10^{4}
18	1×10^{-3}	1/25	1×10^{-3}	2×10^{4}
19	5×10^{-5}	1/20	1×10^{-3}	1×10^{4}
20	7×10^{-5}	1/20	1×10^{-3}	1×10^{4}
21	1×10^{-4}	1/20	1×10^{-3}	1×10^{4}
22	3×10^{-4}	1/20	1×10^{-3}	1×10^{4}
23	5×10^{-4}	1/20	1×10^{-3}	1×10^{4}
24	7×10^{-4}	1/20	1×10^{-3}	1×10^{4}
25	1×10^{-3}	1/20	1×10^{-3}	1×10^{4}
26	1×10^{-3}	1/15	1×10^{-3}	1×10^{4}
27	2×10^{-3}	1/15	1×10^{-3}	1×10^{4}
28	1×10^{-3}	2/15	1×10^{-3}	1×10^{4}
29	1×10^{-4}	1/20	6.4×10^{-4}	1×10^{4}
30	5×10^{-4}	1/20	6.4×10^{-4}	2×10^{4}
31	1×10^{-3}	1/20	6.4×10^{-4}	2×10^{4}
32	1×10^{-3}	2/15	6.4×10^{-4}	1×10^{4}
33	1×10^{-4}	1/20	1×10^{-4}	1×10^{5}
34	5×10^{-4}	1/20	1×10^{-4}	1×10^{5}

3 RESULTS

3.1 Time variation of the gap structures

In this section, we consider the time-variation of gap widths and depths. Here we define the gap width as a radial width of a region where the surface density is smaller than a density threshold $\Sigma_{\rm th}$. In this subsection, we use $\Sigma_{\rm th} = 0.5\Sigma_0$ (in next subsection, we will use other threshold values). Following Fung et al. (2014), we define the gap depth as the space-averaged surface density over the region of $|R - R_p| < \delta$, $\delta = 2\max(R_H, r_p)$, excluding the circumplanetary region in which $|\phi - \phi_p| < \delta/R$, where R_H is the Hill radius[2]. In the following, we label this averaged surface density as follows: $\Sigma'_{\rm min}$[3]. The minimum value of the azimuthally averaged surface density, $\Sigma_{\rm min}$, is smaller than $\Sigma'_{\rm min}$, when there is a deep gap. This difference is addressed in Section 4.

Figure 1 shows the time variation of the gap width and depth (left panel) and a snapshot of the azimuthally averaged surface density (right panel), for $M_{\rm p}/M_* = 10^{-3}$, $\alpha = 10^{-3}$, and $h_{\rm p}/R_{\rm p} = 1/25$. We will first consider the time variation of the gap width. As can be seen in the left panel of

[2] Because the gap structure is almost in steady state, it is not necessary to time-average the surface density.
[3] Fung et al. (2014) use $\Sigma_{\rm gap}$ instead of $\Sigma'_{\rm min}$.

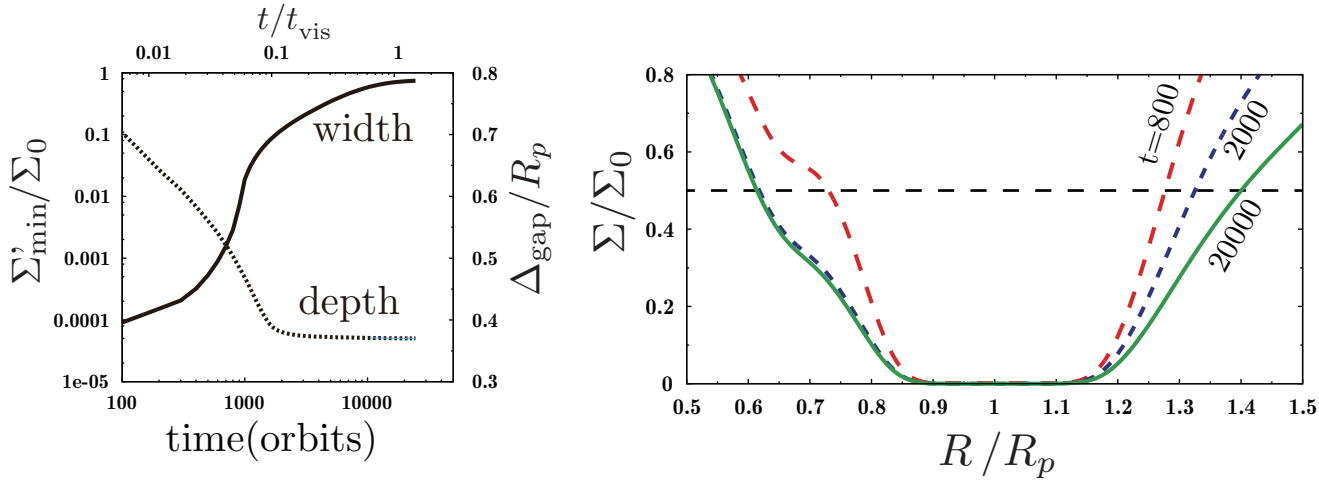

Figure 1. Time variation of the gap structure with $\alpha = 10^{-3}$, $h_{\rm p}/R_{\rm p} = 1/25$, and $M_p/M_* = 10^{-3}$. (*Left)* Time variation of the gap width measured by $\Sigma_{\rm th} = 0.5\Sigma_0$ (solid), and the surface density averaged over the gap bottom (see text; dotted line). (*Right*) Radial distribution of the azimuthally averaged surface density at $t = 800$ (dashed line), 2000 (dotted line), and 20000 (solid line) planetary orbits.

Figure 1, a narrow gap, $\Delta_{\rm gap} = 0.4R_p$, is formed at $t = 100$ planetary orbits. The gap width gradually widens with time. Finally, the gap width reaches $0.79R_p$ at $t \simeq t_{\rm vis} = 1.5 \times 10^4$ planetary orbits. After that, the gap width is almost saturated. The distribution of the azimuthally averaged surface density becomes wider with time as shown in the right panel. Note that the evolution of the surface density is slightly asymmetric with respect to the planet; this may be due to the influence of the inner boundary. However, the gap structure is almost symmetric, as can be seen in the right panel.

The time variation of the gap depth is rapid in comparison with the time variation in the gap width. Until $t = 2000$ planetary orbits, the gap rapidly becomes deeper. After that, the gap depth appears to not significantly change with time. However, the depth gradually increases by a factor of ~ 2 as the gap becomes wider. Note that as with the minimum surface density, the evolution is almost the same as that of $\Sigma'_{\rm min}$.

Figure 2 is similar to Figure 1, but illustrates the time variation of the gap widths and depths for different parameters. As in Figure 1, the gap width and depth reach the saturated value at $t \sim t_{\rm vis}$. For all the cases listed in Table 1, we confirmed that the depth and width of the gap were saturated at the end of each simulation.

3.2 Gap radial profile

Although in the previous section the gap edges were used to define $\Sigma_{\rm th} = 0.5\Sigma_0$, we can use other $\Sigma_{\rm th}$. Adopting $\Sigma_{\rm th} = 0.1\Sigma_0$, $0.3\Sigma_0$, $0.5\Sigma_0$, and $0.8\Sigma_0$, we can measure width with each $\Sigma_{\rm th}$ for a gap, as illustrated in the left panel of Figure 3. The right panel of Figure 3 shows the gap widths with $\Sigma_{\rm th} = 0.1\Sigma_0, 0.3\Sigma_0, 0.5\Sigma_0$, and $0.8\Sigma_0$ in terms of K'. As can be seen in the figure, the gap widths defined by $\Sigma_{\rm th} = 0.1\Sigma_0$ and $0.3\Sigma_0$ are proportional to $K'^{1/4}$, as was seen with $\Sigma_{\rm th} = 0.5\Sigma_0$. Although the gap widths defined by $\Sigma_{\rm th} = 0.8\Sigma_0$ deviate slightly from the line defined by $\propto K'^{1/4}$ for $K' \lesssim 1$, they are roughly proportional to $K'^{1/4}$. Hence, we can derive an empirical relationship for the gap widths defined by $\Sigma_{\rm th}$ in terms of K', as follows:

$$\frac{\Delta_{\rm gap}\left(\Sigma_{\rm th}\right)}{R_{\rm p}} = \left(0.5\frac{\Sigma_{\rm th}}{\Sigma_0} + 0.16\right) K'^{1/4}. \tag{12}$$

Note that the above relationship corresponds to equation (7) when $\Sigma_{\rm th}/\Sigma_0 = 0.5$. Equation (12) is in good agreement with the gap widths shown in Figure 3.

In Figure 4, we illustrate the azimuthal surface density given by the hydrodynamic simulations. Based on the results of our simulations, we can derive an empirical formula for the surface density distribution of the gap, as follows:

$$\Sigma(R) = \begin{cases} \Sigma_{\rm min} & \text{for } |R - R_p| < \Delta R_1, \\ \Sigma_{\rm gap}(R) & \text{for } \Delta R_1 < |R - R_p| < \Delta R_2, \\ \Sigma_0 & \text{for } |R - R_p| > \Delta R_2, \end{cases} \tag{13}$$

with

$$\frac{\Sigma_{\rm gap}(R)}{\Sigma_0} = 4.0K'^{-1/4}\frac{|R - R_{\rm p}|}{R_{\rm p}} - 0.32, \tag{14}$$

where ΔR_1 and ΔR_2 are given by

$$\Delta R_1 = \left(\frac{\Sigma_{\rm min}}{4\Sigma_0} + 0.08\right) K'^{1/4} R_p, \tag{15}$$

$$\Delta R_2 = 0.33K'^{1/4} R_p. \tag{16}$$

According to previous studies (e.g., Duffell & MacFadyen 2013; Fung et al. 2014; Kanagawa et al. 2015a), the surface density of the gap bottom $\Sigma_{\rm min}$ is given by

$$\frac{\Sigma_{\rm min}}{\Sigma_0} = \frac{1}{1 + 0.04K}, \tag{17}$$

where

$$K = \left(\frac{M_{\rm p}}{M_*}\right)^2 \left(\frac{h_{\rm p}}{R_{\rm p}}\right)^{-5} \alpha^{-1}. \tag{18}$$

In the top row of Figure 4, we show the gap structures of $M_{\rm p}/M_* = 5 \times 10^{-4}$ to 10^{-3} for $h_{\rm p}/R_{\rm p} = 1/20$ and $\alpha = 10^{-3}$. For this case, equation (13) accurately reproduces the gap structures obtained by the two-dimensional hydrodynamic simulations. The second and third rows show

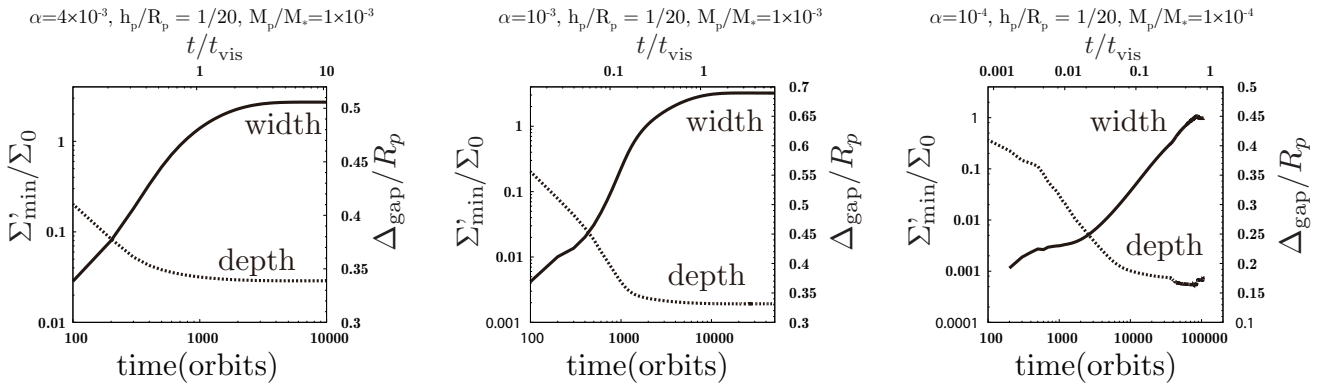

Figure 2. Similar to the left panel of Figure 1, but in the left panel, $\alpha = 4 \times 10^{-3}$, $M_p/M_* = 10^{-3}$; in the middle panel, $\alpha = 10^{-3}$, $M_p/M_* = 10^{-3}$; and in the right panel, $\alpha = 10^{-4}$, $M_p/M_* = 5 \times 10^{-4}$. The disc aspect ratio is set to 1/20.

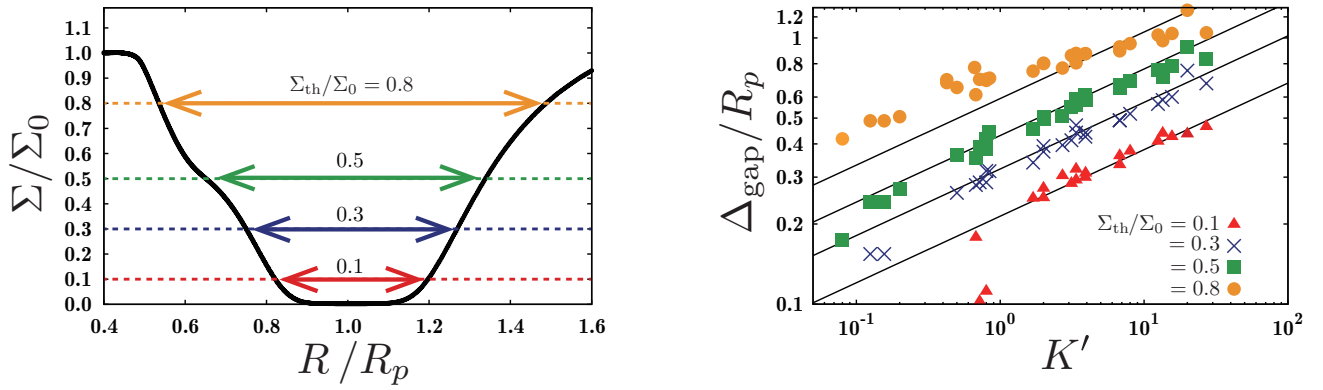

Figure 3. (*Left*) Schematic picture of measurement of the gap widths with various $\Sigma_{\rm th}$. (*Right*) The gap widths with $\Sigma_{\rm th} = 0.1\Sigma_0, 0.3\Sigma_0, 0.5\Sigma_0$, and $0.8\Sigma_0$. The thin lines show the results for equation (12) with $\Sigma_{\rm th} = 0.1\Sigma_0, 0.3\Sigma_0, 0.5\Sigma_0$, and $0.8\Sigma_0$ (from the bottom).

the gap structures of $M_{\rm p}/M_* = 10^{-3}$ and 5×10^{-4} for various disc aspect ratios and viscosities. As in the top row, equation (13) accurately reproduces the results of the hydrodynamic simulations. The bottom row shows the gap structures of $M_{\rm p}/M_* = 10^{-4}$. For $(\alpha, h_{\rm p}/R_{\rm p}) = (10^{-4}, 1/20)$ and $(10^{-3}, 1/25)$, equation (13) is still able to fit the gap structure of the simulations, but for $(\alpha, h_{\rm p}/R_{\rm p}) = (10^{-3}, 1/20)$, the gap obtained by the simulation is wider than that given by the equation. Equation (13) does not give a good estimate when the gap is shallow, that is, $\Sigma_{\rm min} \gtrsim 0.5\Sigma_0$.

The surface density of equation (14) is derived from the empirical formula of equation (12). Hence, the surface density distribution of equation (13) can reproduce the gap widths shown in Figure 3, and it can do this as well as equation (12).

3.3 Comparison with previous studies

We compared our result to those of hydrodynamic simulations in previous studies. Figure 5 shows the gap widths given by our simulations and those of Varnière et al. (2004) and Duffell & MacFadyen (2013). Because these studies used $\Sigma_{\rm th} = 1/3\Sigma_0$ to define the gap width [4], we plot the gap widths as measured by $\Sigma_{\rm th} = 1/3\Sigma_0$. For $K' \lesssim 10$, the gap widths obtained by previous studies increases as $K'^{1/4}$, which is consistent with the results of equation (12). As K' continues to increase, the gap widths given by previous studies have a larger scatter respect our results. In particular, the widths given by Duffell & MacFadyen (2013) are significantly narrower than our results. They mainly investigated situations with very low viscosity, that is, $\alpha \lesssim 10^{-4}$. We here remind the reader of the time variations of the gap width described in Subsection 3.1. The time that the gap reaches the saturated width is estimated by the viscous timescale, as in equation (9). When $\alpha = 10^{-4}$, the time scale is about 10^5, although previous studies estimated this to be several thousand planetary orbits. The variance in the gap width seen in the previous studies can be explained by their short computational times. Note that when the viscosity is very low, because the time scale of equation (9) is very long, the gap cannot reach the saturated width within the lifetime of the disc. In this case, equation (12) underestimates the planet mass.

Recently, Duffell & Chiang (2015) investigated the gap

[4] Strictly speaking, Varnière et al. (2004) adopted $\Sigma_{\rm th} = 0.4\Sigma_0$

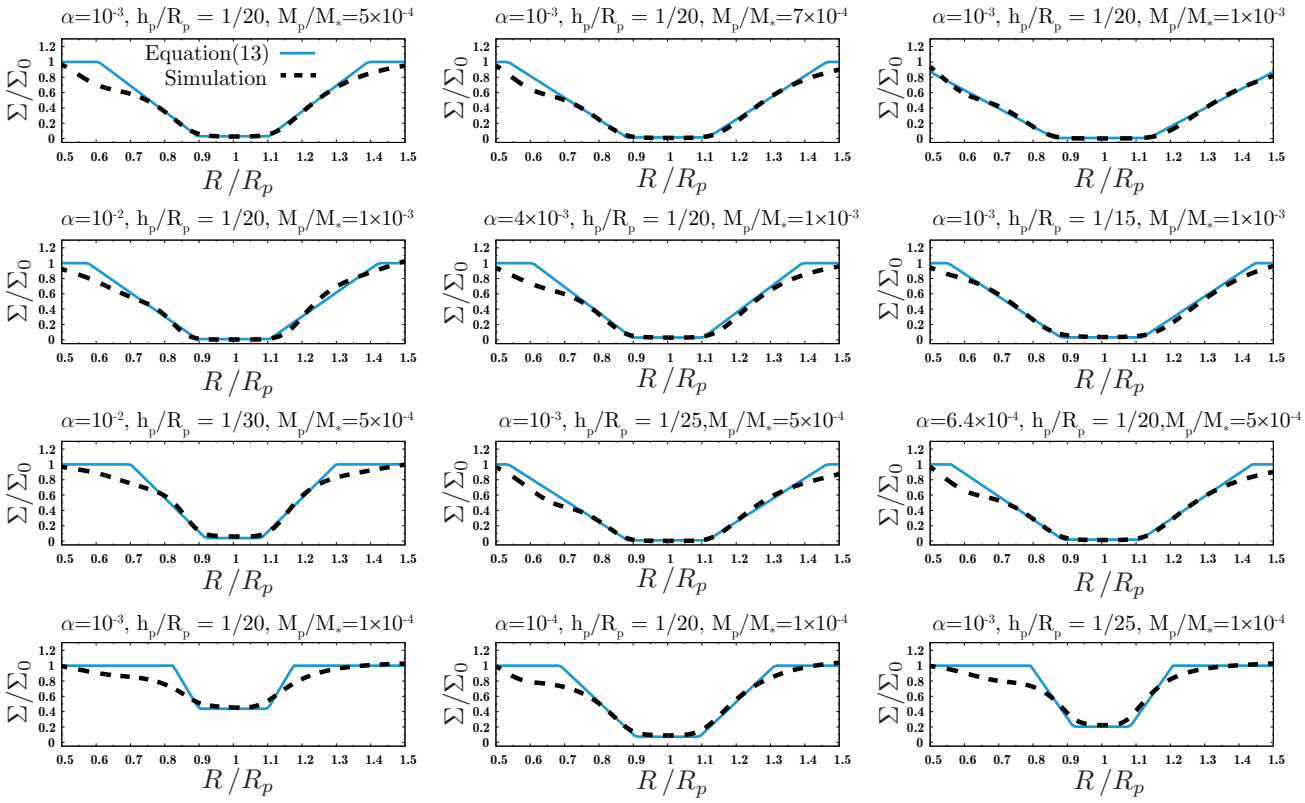

Figure 4. Azimuthally averaged surface densities given by the empirical formula of equation (13) (solid line) and the hydrodynamic simulations (dashed line) for various sets of planet mass, disc aspect ratio, and viscosity.

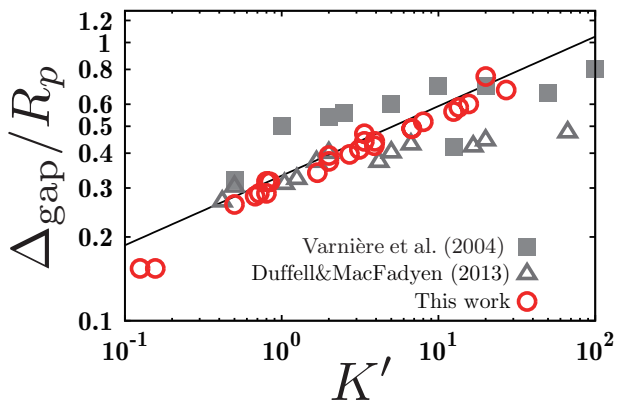

Figure 5. The gap width with $\Sigma_{\rm th} = (1/3)\Sigma_0$ obtained by our simulations (cross), and the gap widths given by Duffell & MacFadyen (2013) (triangle) and Varnière et al. (2004) (square). The thin line indicates the solution to equation (12) with $\Sigma_{\rm th} = (1/3)\Sigma_0$.

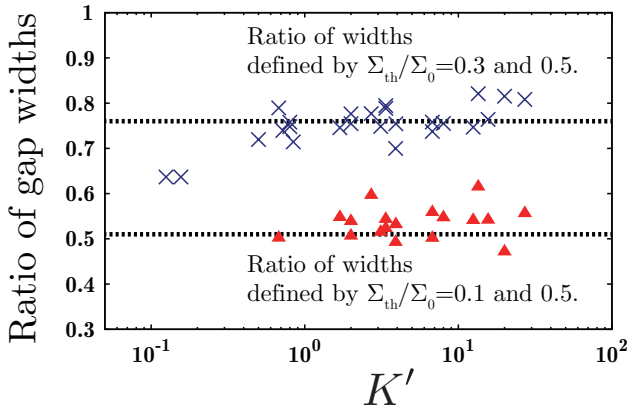

Figure 6. The ratio of the gap width defined by $\Sigma_{\rm th} = 0.1\Sigma_0$ to that defined by $\Sigma_{\rm th} = 0.5\Sigma_0$ (triangles) and $\Sigma_{\rm th} = 0.3\Sigma_0$ and $0.5\Sigma_0$ (crosses). The horizontal dotted lines indicate the values predicted by equation (19).

widths in the viscous case ($\alpha \sim 10^{-3}$). They have measured the gap width using $\Sigma_{\rm th} = 0.1\Sigma_0$ and derived the following empirical formula: $\Delta_{\rm gap}/R_p = 0.5(h_{\rm p}/R_{\rm p})^{0.22}K'^{0.22}$. Their empirical formula is quite similar to equation (12) if $h_{\rm p}/R_{\rm p} = 0.04$; this is because they have primarily considered cases for which $h_{\rm p}/R_{\rm p} \simeq 0.04$.

3.4 Observational applications

3.4.1 Constraint from the gap radial profile

Recently, many gap structures have been discovered by ALMA; these have been found not only in dust (e.g., ALMA Partnership et al. 2015) but also in gas (Yen et al. 2016). Such gap structures in protoplanetary discs can

be created by dust growth (Zhang et al. 2015), sintering (Okuzumi et al. 2016), the effects of MRI (Flock et al. 2015), secular gravitational instability due to gas–dust friction (Takahashi & Inutsuka 2016), and disc–planet interaction. It is difficult to distinguish the origin from observations. However, using the relationship of the gap radial profile that is shown above, we are able to assess whether the observed gap is due to the disc–planet interaction.

Using equation (12), we can determine the ratio of the gap width for any two arbitrary surface densities $\Sigma_{\rm th,a}$ and $\Sigma_{\rm th,b}$ as

$$\frac{\Delta_{\rm gap}(\Sigma_{\rm th,a})}{\Delta_{\rm gap}(\Sigma_{\rm th,b})} = \frac{\Sigma_{\rm th,a}/\Sigma_0 + 0.32}{\Sigma_{\rm th,b}/\Sigma_0 + 0.32}. \tag{19}$$

As can be seen from the above equation, the ratio of the gap widths depends only on the surface densities defined by the widths. In Figure 6, we show two ratios of gap widths, defined by $\Sigma_{\rm th} = 0.1\Sigma_0$ and $0.5\Sigma_0$, and by $\Sigma_{\rm th} = 0.3\Sigma_0$ and $0.5\Sigma_0$. Using equation (6), we obtain that the ratios are 0.51 and 0.76, respectively. As can be seen in the figure, the ratios obtained from the simulations are reasonably consistent with those obtained with equation (19).

3.4.2 Gap depth–width relation

As shown in Kanagawa et al. (2016), there is a relationship between the depth and width of a gap. Combining equations (12) and (17), we can derive this relationship in terms of the locations of $\Sigma_{\rm th}$, as follows:

$$\frac{\Delta_{\rm gap}\left(\Sigma_{\rm th}/\Sigma_0\right)}{R_p}\left(\frac{\Sigma'_{\rm min}}{\Sigma_0-\Sigma'_{\rm min}}\right)^{1/4}\left(\frac{h_{\rm p}}{R_{\rm p}}\right)^{-1/2} = 1.16\frac{\Sigma_{\rm th}}{\Sigma_0}+0.35. \tag{20}$$

If the gap is created by a planet, its width, as measured by the above-surface density, should satisfy equation (20). When the gap structure is completely resolved and the disc aspect ratio is precisely estimated, we can use the gap widths measured by the different surface density at the gap edge and equation (20) to strictly judge whether the gap was created by the planet.

3.4.3 Applicability of the model

We now discuss some considerations when equations (19) and (20) are applied to observations. First, we must consider that the distribution of dust particles may be different from that of a gas when the relations are applied to an observation of dust thermal emissions. Because of dust filtration (e.g., Zhu et al. 2012b; Dipierro et al. 2015; Picogna & Kley 2015; Rosotti et al. 2016), a gap in dust can be deeper and wider than in gas if the size of the dust particles (or the Stokes number of particles) is relatively large. Hence, equations (19) and (20) should be used for observations of disc gas. Alternatively, the dust–gas coupling depends on the gas surface density, as well as on the size of the dust particles. If the gas density is sufficiently large, the gas and dust particles will be well mixed. In this case, equations (19) and (20) would provide a good estimate.

Second, we assume that the gap structure is in steady state. As shown in Section 3.1, the timescale required for the gap to be in steady state can be roughly estimated as $t_{\rm vis} \sim$ 0.1 Myr. If an observed gap is younger than this timescale, the gap will be narrower than it would be in steady state. Such young gaps cannot be estimated by equations (19) and (20).

Finally, we note that equations (19) and (20) should be used for relatively deep gaps. As shown in Figure 3, for a shallow gap ($K' < 1$), the actual gap width measured for a larger surface density is slightly wider than that estimated by equation (20). Because of this, in this case, equation (20) would estimate the disc scale height to be about 1.5 times the actual value.

4 SEMIANALYTICAL MODEL OF RADIAL GAP STRUCTURES

4.1 Formulation

A planet exchanges angular momentum with the surrounding disc gas through density waves. The planet gives angular momentum to density waves. Then, the angular momentum from the planet is carried by the waves. Finally the angular momentum is deposited to the disc gas by dissipation of the waves (Takeuchi et al. 1996; Goodman & Rafikov 2001). This angular momentum transfer via wave propagation is closely connected with the gap structure, as discussed in K15. Duffell (2015) built an analytical model of the gap structure using the wave damping model of Goodman & Rafikov (2001). His model can accurately reproduce the gap structures obtained by two-dimensional hydrodynamic simulations, provided that the gap is shallow. As the gap deepens, the width predicted by his model is much narrower than that obtained by the two-dimensional simulation. Kanagawa et al. (2015a) described the angular momentum deposition using two free parameters $x_{\rm d}$ and $w_{\rm d}$, which represent the position at which waves are damped and the width of the deposition site, respectively. Even for a deep gap, this model can reproduce the gap depth and width obtained by the two-dimensional simulation. However, the gap structure strongly depends on the choice of the parameters $x_{\rm d}$ and $w_{\rm d}$. In this study, we used the results of the hydrodynamic simulations to obtain realistic values of $x_{\rm d}$ and $w_{\rm d}$ for the angular momentum transfer of the waves. Using these values, we are able to construct a semianalytical gap model based on the results of K15.

We used the basic equations for the two-dimensional hydrodynamic simulations to derive the basic equation for the one-dimensional model. Combining equations (1) and (3), the equation of angular momentum becomes

$$\frac{\partial R\Sigma \mathrm{v}_\phi}{\partial t} + \frac{1}{R}\frac{\partial\left(R^2\Sigma \mathrm{v}_\phi \mathrm{v}_{\rm R}\right)}{\partial R} + \frac{\partial \Sigma \mathrm{v}_\phi^2}{\partial \phi} = -c^2\frac{\partial \Sigma}{\partial \phi} - \Sigma\frac{\partial \Psi}{\partial \phi} + Rf_\phi. \tag{21}$$

We assumed that background structure is axisymmetric and rotates with a constant angular velocity, while the perturbed structure (wave) is nonaxisymmetric and rotates with an angular velocity that depends on R and ϕ. Hence, we can decompose the azimuthal velocity into two parts, the background and the perturbation (Muto et al. 2010):

$$\mathrm{v}_\phi = \mathrm{v}_\phi^{\rm avg}(\mathrm{R}) + \delta \mathrm{v}_\phi(\mathrm{R},\phi). \tag{22}$$

Note that equation (22) is not a linear approximation. The

azimuthally averaged version of equation (21) can be written as

$$\frac{\partial R\overline{\Sigma v_\phi}}{\partial t}+\frac{1}{2\pi R}\frac{\partial F_J}{\partial R}=-\frac{1}{2\pi R}\frac{dT_{\rm p}}{dR}, \tag{23}$$

where F_J is the azimuthally averaged angular momentum flux,

$$F_J(R)=Rv_\phi^{\rm avg}({\rm R})\Sigma_{\rm M}+{\rm F}_{\rm J}^{\rm wave}({\rm R})+{\rm F}_{\rm J}^{\rm vis}({\rm R}), \tag{24}$$

in which where the first term is the angular momentum flux induced by an axisymmetric advection, and the azimuthally averaged mass flux F_M is $2\pi R\overline{\Sigma v_{\rm R}}$. The angular momentum fluxes due to nonaxisymmetric advection (waves) $F_J^{\rm wave}$ and viscous diffusion $F_J^{\rm vis}$ are respectively defined by

$$F_J^{\rm wave}=2\pi R^2\overline{\Sigma\delta v_\phi v_{\rm R}}, \tag{25}$$

$$F_J^{\rm vis}=2\pi R^3\overline{\nu\Sigma\frac{\partial\Omega}{\partial R}}+2\pi R\overline{\nu\Sigma\frac{\partial v_{\rm R}}{\partial\phi}}. \tag{26}$$

Note that the second term of $F_J^{\rm vis}$ in equation (26) is negligible (see Appendix A), and we will neglect it below. The right-hand side of equation (23) represents the gravitational torque excited by the planet. The azimuthally averaged mass flux denoted by F_M is defined to be $\overline{\Sigma v_{\rm R}}$. The torque density on the right-hand side of equation (23) is obtained as follows:

$$\frac{dT_{\rm p}}{dR}=2\pi R\overline{\Sigma\frac{\partial\Psi}{\partial\phi}}, \tag{27}$$

and therefore the torque exerted by the planet is

$$T_{\rm p}(R)=\int_{R_{\rm p}}^{R}\frac{dT_{\rm p}}{dR}dR=2\pi\int_{R_{\rm p}}^{R}\overline{\Sigma\frac{\partial\Psi}{\partial\phi}}RdR. \tag{28}$$

To clarify the effect of the wave propagation, equation (23) can be rewritten as

$$\frac{\partial R\overline{\Sigma v_\phi}}{\partial t}+\frac{1}{2\pi R}\frac{\partial\left(Rv_\phi^{\rm avg}\Sigma_{\rm M}\right)}{\partial R}+\frac{1}{2\pi R}\frac{\partial F_J^{\rm vis}}{\partial R}=-\frac{1}{2\pi R}\left(\frac{dT_{\rm p}}{dR}-\frac{dF_J^{\rm wave}}{dR}\right). \tag{29}$$

First, the planet excites the waves and thus transfers angular momentum to them. Next, this angular momentum is deposited onto the disc as the waves are damped. Because of this wave propagation, the deposition rate of angular momentum to the disc gas is different from the torque density excited by the planet. The deposition rate from the waves is given by

$$\Lambda_{\rm d}(R)=\frac{dT_{\rm p}}{dR}-\frac{dF_J^{\rm wave}}{dR}. \tag{30}$$

In Figure 7, we show a schematic picture of the effect of the wave propagation, as discussed above. Because of the wave propagation, the distribution of the torque density deposited onto the disc is different from the distribution of the torque density exerted by the planet. The deposition torque to the disc is obtained by the difference between the planetary torque and the angular momentum flux due to the waves as illustrated in the bottom panel of Figure 7. This is obtained as follows:

$$T_{\rm d}(R)=\int_{R_{\rm p}}^{R}\Lambda_d(R')dR'=T_{\rm p}(R)-F_J^{\rm wave}(R). \tag{31}$$

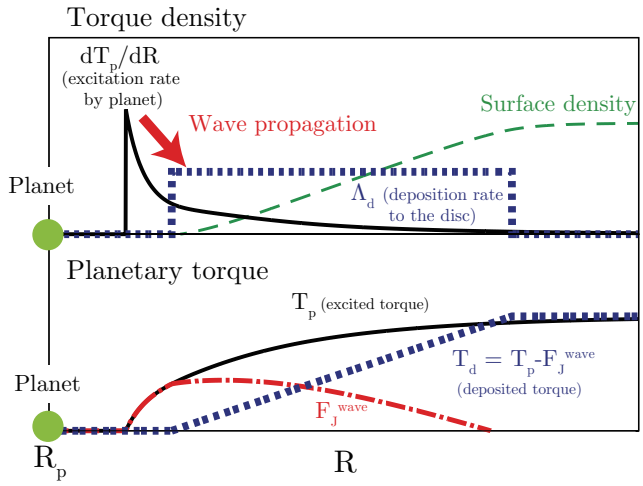

Figure 7. Schematic picture of the angular momentum transfer due to the density waves. In the top panel, two torque densities are illustrated: excitation rate of the planetary torque, $dT_{\rm p}/dR$, (equation 27), and the deposition rate of the planetary torque due to the disc (equation 30), $\Lambda_{\rm d}$. The bottom panel is similar to the top panel but shows the integrated values, that is, the torque excited by the planet (equation 28) and the torque deposited on the disc (equation 31). Because the waves carry the angular momentum ($F_J^{\rm wave}$), the distribution of the deposition torque differs from that of the excitation torque, as shown in the top panel. The torque felt by the disc gas corresponds to the deposited torque (see equation 33).

Integrating equation (23), we obtain an equation for the angular momentum flux, as follows:

$$Rv_\phi^{\rm avg}\Sigma_{\rm M}+{\rm F}_{\rm J}^{\rm vis}=F_J(R_{\rm p})+T_{\rm p}-F_J^{\rm wave}-\int_{R_{\rm p}}^{R}\frac{\partial R^2\overline{\Sigma v_\phi}}{\partial t}RdR. \tag{32}$$

In steady state, the last term on the right-hand side of equation (32) should be zero. Hence, we finally obtain

$$Rv_\phi^{\rm avg}\Sigma_{\rm M}+{\rm F}_{\rm J}^{\rm vis}({\rm R})={\rm F}_{\rm J}({\rm R}_{\rm p})+{\rm T}_{\rm d}({\rm R}), \tag{33}$$

which is the same as the basic equation (equation 9) of K15.

Considering the deviation from the Keplerian angular velocity and the violation of the Rayleigh condition, in K15, they solved equation (33) under a local approximation; we will do this below. Although the gap may not be narrow enough to apply the local approximation, we will neglect the terms that are proportional to $h_{\rm p}/R_{\rm p}$ and higher order terms. We should note that the model for Λ_d would include this discrepancy. To consider a wide gap, we must solve equation (33) without the local approximation. As seen below, however, we can obtain reasonably consistent results.

4.2 Model of wave excitation

We adopt the WKB formula for the planetary torque density (e.g., Ward 1986) and use a simple cutoff, as in K15:

$$\frac{dT_{\rm p}}{dR}=\begin{cases}\pm0.40f_{\rm NL}\dfrac{\Sigma(R)}{\Sigma_0}\left(\dfrac{h_{\rm p}}{R-R_{\rm p}}\right)^4\left(\dfrac{dT_{\rm p}}{dR}\right)_0 & \text{for } |R-R_{\rm p}|>\Delta,\\ 0 & \text{for } |R-R_{\rm p}|\leqslant\Delta,\end{cases} \tag{34}$$

where

$$\left(\frac{dT_{\rm p}}{dR}\right)_0 = 2\pi R_{\rm p}^3 \Omega_p^2 \Sigma_0 \left(\frac{M_{\rm p}}{M_*}\right)^2 \left(\frac{h_{\rm p}}{R_{\rm p}}\right)^{-4}. \quad (35)$$

For the $\pm$ sign in equation (34), $+$ is taken for $R > R_{\rm p}$ and $-$ is taken for $R < R_{\rm p}$. The cutoff length Δ should set to $1.3h_{\rm p}$ to match the one-side torque obtained from linear analyses of the disc–planet interaction (Takeuchi & Miyama 1998; Tanaka et al. 2002; Muto & Inutsuka 2009). If the planet is large as $M_p \gtrsim (h_{\rm p}/R_{\rm p})^3$, the excitation of density waves is in the nonlinear regime (e.g., Ward 1997). The factor $f_{\rm NL}$ represents the rate of reduction of the planetary torque due to nonlinear effects, because these would make the excitation torque smaller than that predicted by linear theory, as shown in Miyoshi et al. (1999). As shown below, $f_{\rm NL} = 0.4$ better reproduces the gap depth obtained by the numerical hydrodynamic simulations. Because we wish to consider cases for which $M_p > (h_{\rm p}/R_{\rm p})^3$, the factor $f_{\rm NL}$ is always set to 0.4.

4.3 Models of wave propagation and angular momentum deposition

In order to solve equation (33), we need to provide a model for Λ_d. In K15, Λ_d was defined in terms of the parameters $x_{\rm d}$ and $w_{\rm d}$[5], as

$$\Lambda_d(R) = \begin{cases} \pm\dfrac{T_{\rm p}^{\infty}}{w_{\rm d}} & \text{for } x_{\rm d} - \frac{w_{\rm d}}{2} < |R - R_{\rm p}| < x_{\rm d} + \frac{w_{\rm d}}{2}, \\ 0 & \text{otherwise,} \end{cases} \quad (36)$$

where the plus sign is taken when $R > R_{\rm p}$, and the minus sign is taken when $R < R_{\rm p}$. The one-side torque exerted by the planet is given by

$$T_{\rm p}^{\infty} = T_{\rm p}(\infty) = 2\pi \int_{R_{\rm p}}^{R\to\infty} \overline{\Sigma \frac{\partial \Psi}{\partial \phi}} R' dR'. \quad (37)$$

The parameters $x_{\rm d}$ and $w_{\rm d}$ are empirically determined by

$$x_{\rm d} = R_{\rm p} \pm \frac{\Delta R_2 + \Delta R_1}{2}, \quad (38)$$

$$w_{\rm d} = \Delta R_2 - \Delta R_1, \quad (39)$$

where ΔR_1 and ΔR_2 are defined by equations (15) and (16), respectively, and the sign of $x_{\rm d}$ is positive when $R > R_{\rm p}$ and negative when $R < R_{\rm p}$. By integrating equation (36), the deposition toque $T_{\rm d}$ is obtained as

$$T_{\rm d}(R) = \begin{cases} 0 & \text{for } |R - R_{\rm p}| < x_{\rm d} - \frac{w_{\rm d}}{2}, \\ \dfrac{T_{\rm p}^{\infty}}{w_{\rm d}} \left| R - \left(x_{\rm d} - \frac{w_{\rm d}}{2}\right) \right| & \text{for } x_{\rm d} - \frac{w_{\rm d}}{2} < |R - R_{\rm p}| < x_{\rm d} + \frac{w_{\rm d}}{2}, \\ T_{\rm p}^{\infty} & \text{for } |R - R_{\rm p}| > x_{\rm d} + \frac{w_{\rm d}}{2}. \end{cases} \quad (40)$$

The one-side torque $T_{\rm p}^{\infty}$ depends on the surface density, as seen in equation (37). Hence, when we solve equation (33), iteration is necessary in order to consistently obtain Σ and Λ_d (or $T_{\rm d}$). For details, see Section 2.4 in K15.

[5] For simplicity, we redefine $x_{\rm d}$ and $w_{\rm d}$ by multiplying those in K15 by $h_{\rm p}$

4.4 Normalization of the torque

The torque exerted by the planet is usually normalized by T_0 (e.g., Baruteau et al. 2014), where

$$T_0 = 2\pi R_{\rm p}^4 \Omega_p^2 \Sigma_0 \left(\frac{M_{\rm p}}{M_*}\right)^2 \left(\frac{h_{\rm p}}{R_{\rm p}}\right)^{-3}. \quad (41)$$

As can be seen in the above equation, T_0 is proportional to the unperturbed surface density Σ_0. However, due to the gap formation, the surface density within the gap significantly decreases. Because of the decrease in the surface density, the planetary torque decreases with $\Sigma_{\rm min}$ (given by equation 17) as $T_0(\Sigma_{\rm min}/\Sigma_0)$ if the torque is primarily exerted on the gap bottom. Hence, we normalize the torque as follows:

$$\frac{T_0}{K} = 2\pi R_{\rm p}^4 \Omega_p^2 \Sigma_0 \left(\frac{h_{\rm p}}{R_{\rm p}}\right)^2 \alpha. \quad (42)$$

As will be shown below, this normalization scales the torques obtained by the hydrodynamic simulations to reasonable values.

4.5 Radial gap structures

We now show the radial structure of a gap, as given by solving equation (33) with a local approximation, as in K15. Figure 8 shows the surface density obtained by solving equation (33) and the azimuthally averaged surface density obtained by the two-dimensional hydrodynamic simulations. As can be seen in the figure, the solutions of equation (33) are in good agreement with the hydrodynamic simulations for various disc scale heights and viscosities, as long as the planet mass is relatively large. In the case of $M_{\rm p}/M_* = 10^{-4}$ with $\alpha = 10^{-3}$ and $h_{\rm p}/R_{\rm p} = 1/25$, the solution of equation (33) gives us a shallower gap than that obtained by the simulations.

Figure 9 shows the torque deposited onto the disc for equation (33) and the two-dimensional hydrodynamic simulations. As with Figure 8, the deposited torque given by equation (40) and the hydrodynamic simulation are reasonably consistent with each other.

The left panel of Figure 10 shows the minimum surface density of the azimuthally averaged surface density $\Sigma_{\rm min}$ versus the parameter K. In the figure, we show $\Sigma_{\rm min}$ as obtained by the solutions of equation (33) with $f_{\rm NL} = 0.4$ and 1.0, and those from the two-dimensional hydrodynamic simulations. For $K < 100$, $\Sigma_{\rm min}$ obtained by the models and the simulations are quite similar to each other, and they are consistent with equation (17). For $K > 100$, with equation (33) and $f_{\rm NL} = 1$, $\Sigma_{\rm min}$ decreases quickly with increasing K, and this gap is much deeper than that obtained in the simulation. On the other hand, the solutions of equation (33) with $f_{\rm NL} = 0.4$ give values of $\Sigma_{\rm min}$ that are reasonably consistent with those obtained in the simulations, even for a relatively large value of K ($K \sim 10^4$). Hence, the assumption of $f_{\rm NL} \simeq 0.4$ would be reasonable for the reduction of the torque due to nonlinearity.

As can be seen in the figure, when K is large, the values of $\Sigma_{\rm min}$ obtained in the simulations are actually smaller than these predicted by equation (17); however, in this case, the surface density averaged throughout the gap bottom region $\Sigma'_{\rm min}$ is consistent with equation (17), as seen in the right panel of Figure 10. In practice, averaging the gap depth over

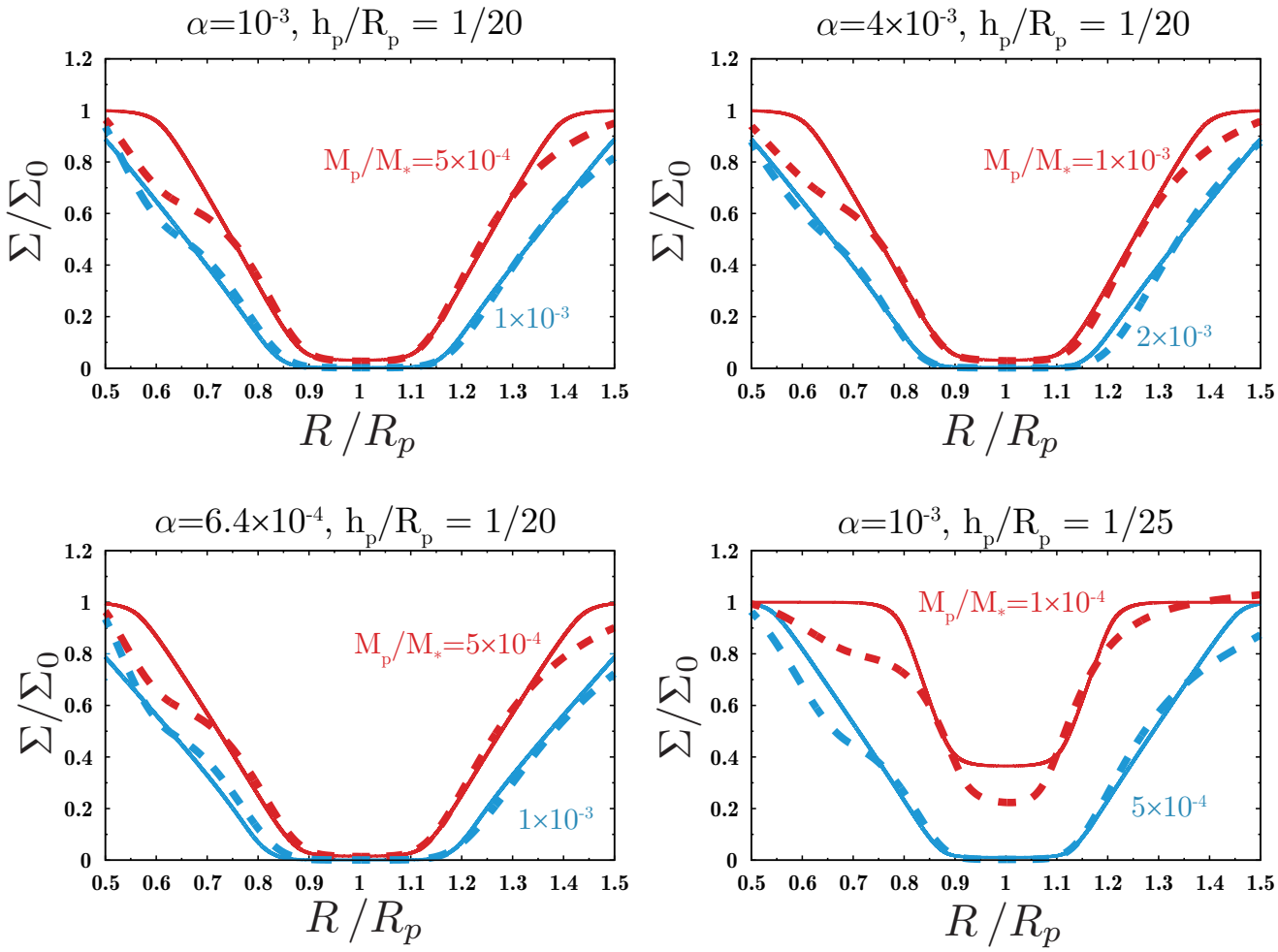

Figure 8. Surface densities obtained by equation (33) (solid lines) and the hydrodynamic simulations (dashed lines).

the bottom would be more meaningful than the depth defined by the minimum surface density, because the minimum surface density is quite small, and in this case, the bottom region is not as wide. The region very close to the planet does not contribute to the gas accretion onto the planet or to the planetary migration. According to Tanigawa & Watanabe (2002), the disc gas accreting onto the planet comes from a location that is twice the Hill radius from the planet. Hence, the gap width defined by the averaging is meaningful for the gas accretion. Furthermore, because the narrow region is smoothed by the beam size of the observation, averaging the gap depth over the bottom region would be useful for interpreting observations.

Thus, the surface density produced by equation (33) is able to reproduce that obtained by the two-dimensional hydrodynamic simulations, provided that the planet mass is relatively large ($M_{\rm p}/M_* \gtrsim 10^{-4}$), as seen in Figure 8. The distribution of the torque deposited from the waves to the disc is also consistent with equation (36) and the hydrodynamic simulations, when the planet is relatively large (Figure 9). Especially for a large K, the nonlinear effects of the wave excitation, $f_{\rm NL} = 0.4$ in the excitation torque of equation (34), result in gap depths that are reasonably consistent with the solutions of equation (33) and the hydrodynamic simulations (Figure 10).

5 WAVE EXCITATION AND PROPAGATION WITH DEEP GAPS

5.1 Planetary torque and angular momentum deposition in the disc

The wave excitation and propagation are crucial process for determining the gap structure by the planet, as discussed in the previous section, and they are qualitatively different depending on the planet mass. In this section, we discuss the dependence of the wave excitation and propagation on the planet mass.

In Figure 11, we show the planetary torque $T_{\rm p}$, the angular momentum flux of the waves $F_J^{\rm wave}$, and the deposited torque $T_{\rm d}$ for a small planet ($M_{\rm p}/M_* = 10^{-4}$), a planet with moderate mass (5×10^{-4}), and a giant planet (10^{-3}). The disc aspect ratio and the viscosity are 1/20 and 10^{-3}, respectively.

In the case of $M_{\rm p}/M_* = 10^{-4}$ (left panel of Figure 11), the wave excitation is in the linear regime. In this case, $T_{\rm p}$ increases within the gap bottom region of $\Sigma \simeq \Sigma_{\rm min}$, and at a

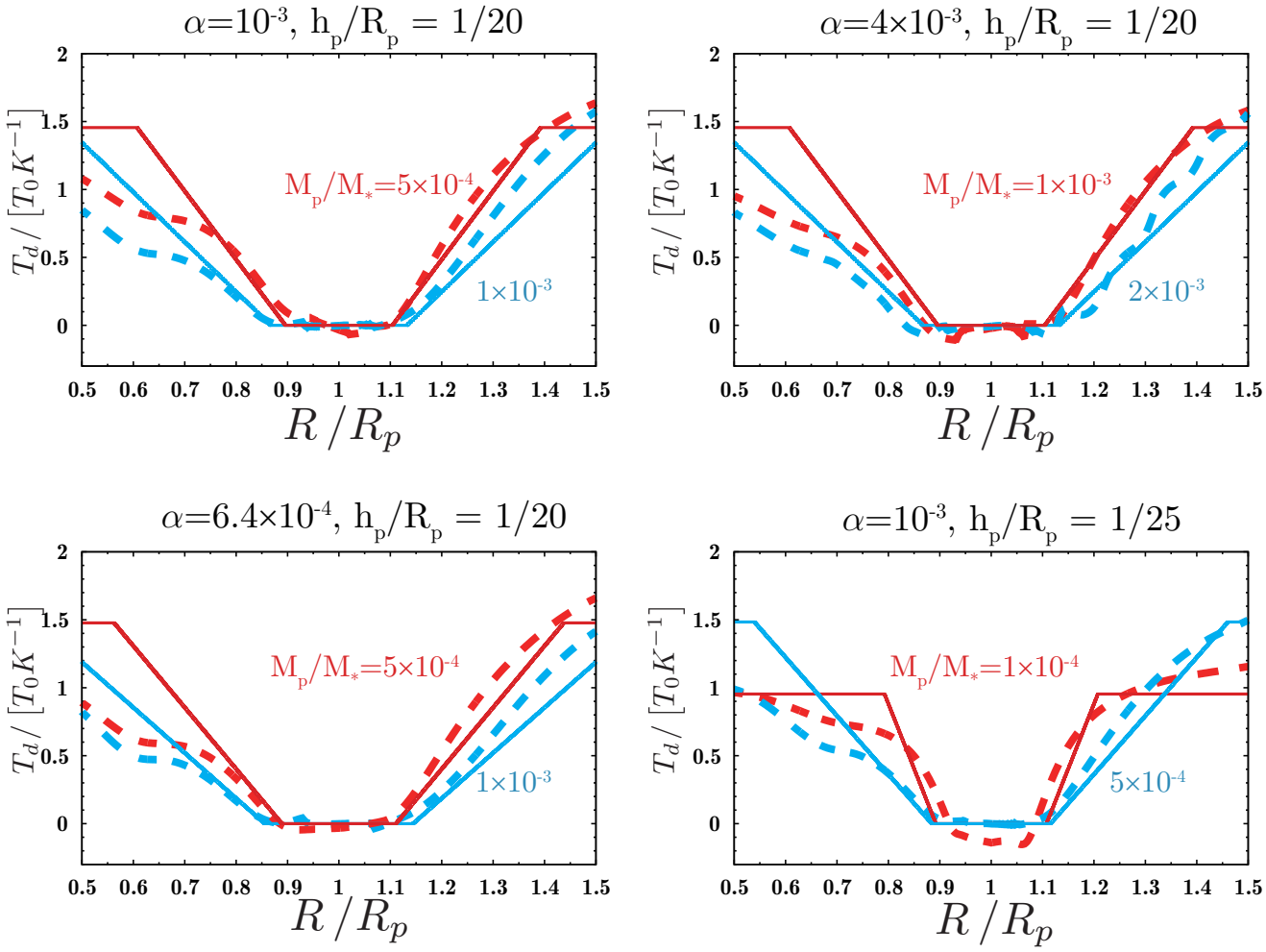

Figure 9. Torque deposited onto the disc, as obtained by equation (40)(solid lines) and the hydrodynamic simulations (dashed lines).

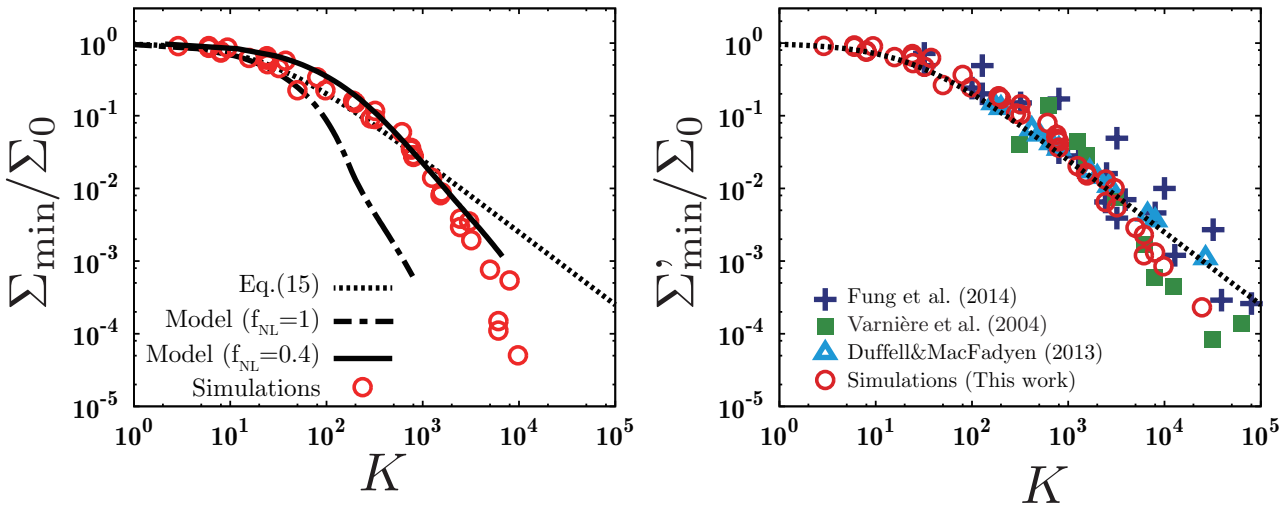

Figure 10. (*Left*) Minimum surface density of the azimuthally averaged surface density $\Sigma_{\rm min}$ versus the parameter K. The circles indicate $\Sigma_{\rm min}$ as given by the two-dimensional hydrodynamic simulations. The dotted line shows equation (17), and the solid and chain lines indicate $\Sigma_{\rm min}$, as given by the solution of equation (33) with $f_{\rm NL}$ = 0.4 and 1.0, respectively. (*Right*) Surface density averaged throughout the gap bottom $\Sigma'_{\rm min}$, as given by our simulations (circles). The crosses, squares, and triangles are the gap depths given by Fung et al. (2014), Varnière et al. (2004), and Duffell & Chiang (2015), respectively.

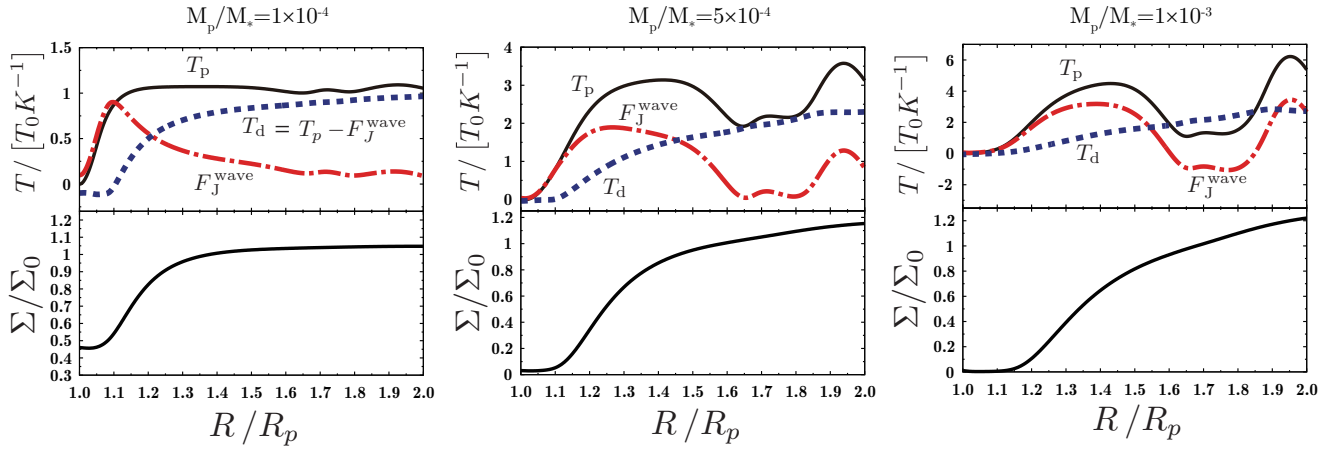

Figure 11. (*Top*) Planetary torque ($T_{\rm p}$, solid line), angular momentum carried by the waves ($F_J^{\rm wave}$, chain line), and deposited torque ($T_{\rm d}$, dotted line) for $M_{\rm p}/M_* = 10^{-4}$ (left), 5×10^{-4} (middle), and 10^{-3} (right). The disc aspect ratio and viscosity were set to 1/20 and 10^{-3}, respectively. (*Bottom*) Azimuthally averaged surface density distribution in each case.

site distant from the planet, it is saturated. The angular momentum flux of the waves $F_J^{\rm wave}$ also increases with the planetary torque when $R/R_{\rm p} \lesssim 1.1$, and then it decreases along with wave damping. By damping the waves, the deposited torque increases in the vicinity of the planet. In this case, the wave excitation is consistent with the linear theory of Goldreich & Tremaine (1980), and the waves are damped by weak shock, as in the model of Goodman & Rafikov (2001). Hence equations (36) and (40) are not very good approximations in this shallow gap case.

When $M_{\rm p}/M_* = 5 \times 10^{-4}$ (the middle panel in Figure 11), the evolution of the waves should be in the nonlinear regime. In this case, the planetary torque increases not only at the gap bottom but also at the gap edge of $\Sigma \sim \Sigma_0$. The angular momentum flux of the waves is almost equal to $T_{\rm p}$ when $R/R_{\rm p} < 1.15$. For $R/R_{\rm p} > 1.15$, $F_J^{\rm wave}$ deviates from $T_{\rm p}$ and decreases. However, the decrease in the $F_J^{\rm wave}$ is much slower than it is in the case of a small planet. Because of this, the increase in the deposited torque is also much slower than in the small planet case. Moreover, at sites far from the planet ($R/R_{\rm p} \simeq 1.7$), $T_{\rm p}$ and $F_J^{\rm wave}$ significantly decrease and increase, respectively, which indicates that the disc–planet interaction occurs even there.

In the right panel of Figure 11, the planet mass is $M_{\rm p}/M_* = 10^{-3}$, and the excitation of waves is highly nonlinear. As in the case of a moderate planet, the planetary torque increases at the gap edge, as well as the gap bottom. The decrease in $F_J^{\rm wave}$ and the increase in $T_{\rm d}$ are slower than in the case of a moderate planet mass. In particular, $T_{\rm d}$ increases to a site very distant from the planet as $R/R_{\rm p} \sim 2$. The planetary torque and the angular momentum flux of the waves also increase and decrease, respectively, at sites distant from the planet (around $R/R_{\rm p} = 1.7$), as in the case of a moderate planet mass.

As shown above, the wave excitation and the angular momentum deposition are qualitatively different in the linear and nonlinear regimes. For a small planet, the disc–planet interaction occurs only in the vicinity of the planet, and the angular momentum flux of the waves decreases quickly around the planet. On the other hand, for a large planet, the disc–planet interaction occurs even at locations far from the planet, and the decrease in the angular momentum flux due to the waves slows down as the planet mass increases. As a result, the deposited torque is distributed to sites that are far from the planet. The disc–planet interaction that occurs at distant sites originates from the interactions acting on the low-numbered resonances, such as the $m = 2$ resonance, which are located at $R/R_{\rm p} = 1.59$. In addition, as shown in Juhász et al. (2015) and Fung & Dong (2015), a large planet can excite secondary waves near the $m = 2$ resonance, and this would affect the angular momentum transfer. Below, we investigate the effect of the interaction due to the resonance of waves with small numbers.

5.2 Wave excitation and damping in low-m modes

To examine the effect of the interactions on the m-th resonances, we consider the Fourier components for Σ, $\mathrm{v_R}$, v_ϕ, and Ψ which are given by

$$f_m(R,m) = \frac{1}{2\pi}\int_0^{2\pi} f(R,\phi)\exp\left(-im\phi\right)d\phi, \tag{43}$$

where f is Σ, $\mathrm{v_R}$, v_ϕ, or Ψ. For convenience, we will let the subscript m indicate the m-th Fourier component. The torque density exerted on the m-th resonance is given by (Goldreich & Tremaine 1980)

$$\left(\frac{dT_{\rm p}}{dR}\right)_m = 4\pi R \Re(\Psi_m)\Im(\Sigma_m), \tag{44}$$

and the integrated torque exerted on the m-th resonance is given by

$$T_{{\rm p},m} = \int_{R_{\rm p}}^{R}\left(\frac{dT_{\rm p}}{dR}\right)_m dR = \int_{R_{\rm p}}^{R} 4\pi R \Re(\Psi_m)\Im(\Sigma_m) dR. \tag{45}$$

The angular momentum carried by the m-th mode of the wave is

$$F_{J,m}^{\rm wave} = 4\pi R^2\left[\Re(\Sigma \mathrm{v_{R,m}})\Re(\delta \mathrm{v}_{\phi,\mathrm{m}}) + \Im(\Sigma \mathrm{v_{R,m}})\Im(\delta \mathrm{v}_{\phi,\mathrm{m}})\right]. \tag{46}$$

The deposited torque on the m-th resonance $T_{{\rm d},m}$ can be written as

$$T_{{\rm d},m} = T_{{\rm p},m} - F_{J,m}^{\rm wave}. \tag{47}$$

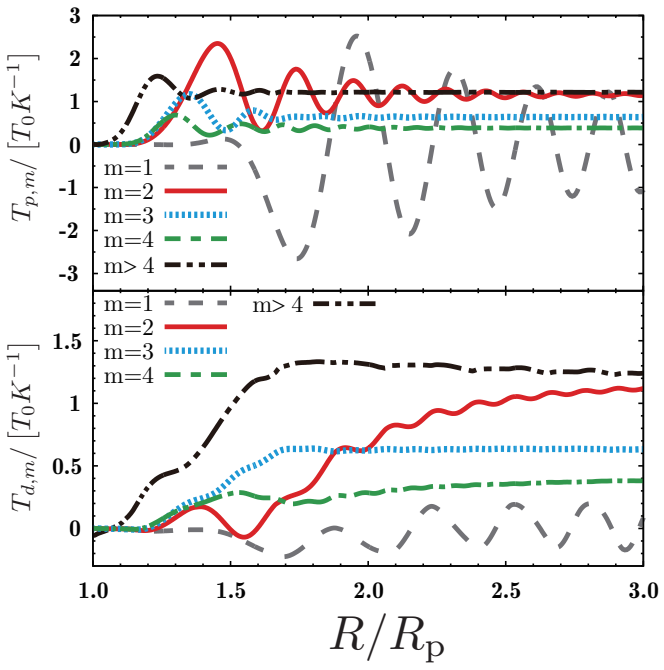

Figure 12. Contributions of the planetary torque (top panel) and deposited torque (bottom panel) from the following resonances: $m = 1$ (dashed), $m = 2$ (solid), $m = 3$ (dotted), and $m = 4$ (chain), in the case of $M_{\rm p}/M_* = 10^{-3}$, $h_{\rm p}/R_{\rm p} = 1/20$, and $\alpha = 10^{-3}$. The double chain line is the sum of the contribution when $m > 4$.

Figure 12 shows the contributions of the planetary torques and the deposited torques due to the lower-order resonances, for the case of $M_{\rm p}/M_* = 10^{-3}$. As a comparison, we also plotted the sum of the contributions from the components for which $m > 4$. For both the planetary torque and the deposited torque, the contributions from the low-m components ($m \leqslant 4$) are as significant as those from the high-m components ($m > 4$). For the planetary torque, the $m = 1$ contributions oscillate around zero at distant locations. As seen in equation (6), the indirect term, which is connected to the gravitational interaction between the planet and the central star, dominates the gravitational potential at sites distant from the planet. The oscillation of the planetary torque is due to the effect of the indirect term. The torques due to the other lower-order resonances are excited from the gap edge ($R/R_{\rm p} \simeq 1.3$) to the outside of the gap ($R/R_{\rm p} \simeq 1.5$). The peak of the torque is located at a more distant site when m is smaller. In particular, the $m = 2$ torque is the largest, which may be a consequence of the nonlinear effects, which can enhance the interaction when the wave number is even (Artymowicz & Lubow 1992; Lee 2016).

For the deposited torque, the $m = 1$ contribution oscillates around zero when $R/R_{\rm p} \gtrsim 1.5$, as in the planetary torque. The deposited torque when $m = 3$ or 4 is distributed away from the gap edge ($R/R_{\rm p} \simeq 1.2$) to the outside of the gap ($R/R_{\rm p} = 1.8$ for $m = 3$, $R/R_{\rm p} = 1.5$ for $m = 4$). In the case of $m = 2$, the deposited torque increases along with the deposited torques for $m = 3$ and 4, and it then decreases from $R/R_{\rm p} = 1.4$ to $R/R_{\rm p} = 1.5$. Outside of this, the deposited torque for $m = 2$ slowly increases again to sites very distant from the planet ($R/R_{\rm p} > 2$). The contribution from the $m = 1$ component oscillates around zero at distant sites, as with the planetary torque. However, the amplitude of the oscillation is much smaller than that of the planetary torque. In the deposition of the angular momentum, the $m = 1$ component would not be important.

When the planet mass is large, the contributions from both the lower-order and high-order resonances are significant. On the other hand, when the planet mass is small, the contributions from the lower-order resonances are negligible compared to those from the higher-order resonances, as with the linear theory. As the planet mass increases, the contributions from the lower-order resonances become more significant. We discuss the details of this in Appendix B.

The development of the $m = 1, 2$ contributions significantly changes the morphology of the waves, and the transfer of angular momentum. In Figure 13, we show the surface density produced by the $m = 1, 2$ components and the sum of the $m > 2$ components, for the same case as shown in Figure 12. The surface density produced by the m-th component is

$$\Sigma(m, R, \phi) = 2\pi\Sigma_m(R, \phi)\exp(im\phi)\,, \tag{48}$$

where Σ_m is the Fourier component of the surface density. The waves that are far from the planet are created by the contributions from the $m = 1$ and $m = 2$ resonances. In particular, the secondary wave that is launched from the site opposite the planet is mainly composed of the $m = 1$ and $m = 2$ components. Because the contribution from the $m = 2$ component is strong, the secondary wave originates at a site opposite from the planet. Fung & Dong (2015) have shown that the azimuthal separation of the primary and secondary waves depends on the planet mass. For a large planet, as shown in Figure 13, this separation is close to 180°, which is consistent with our results. For a smaller planet, the separation is smaller than 180°. In this case, the contributions from other lower modes (e.g., $m = 3, 4$), are not much smaller than these from $m = 1, 2$ (see Appendix B). Because of these contributions, the launching point of the secondary wave would move toward the planet.

It is worth noting that the secondary wave interacts with the planet. As seen in Figure 13, the secondary wave passes through the location at which $\phi = \phi_p$ around $R/R_{\rm p} = 1.4$. Near this location, the planetary torque due to the $m = 2$ resonance increases and then decreases, as shown in the top panel of Figure 12; this is a result of the interaction between the planet and the secondary wave. The deposited torque of $m = 2$ also increases and decreases when the secondary wave passes through the location at which $\phi = \phi_p$; this is also a consequence of the interaction between the planet and the secondary wave, and especially of the $m = 2$ component.

6 SUMMARY AND DISCUSSION

We made a survey of the wide parameter space by performing 34 runs of a hydrodynamic simulation, and we derived a quantitative relationship between a planet and the gap radial profile. We used the results of the simulations to obtain an empirical model of the wave propagation. Using this empirical model, we constructed a semianalytical model of the gap structure, and it is in very good agreement with the

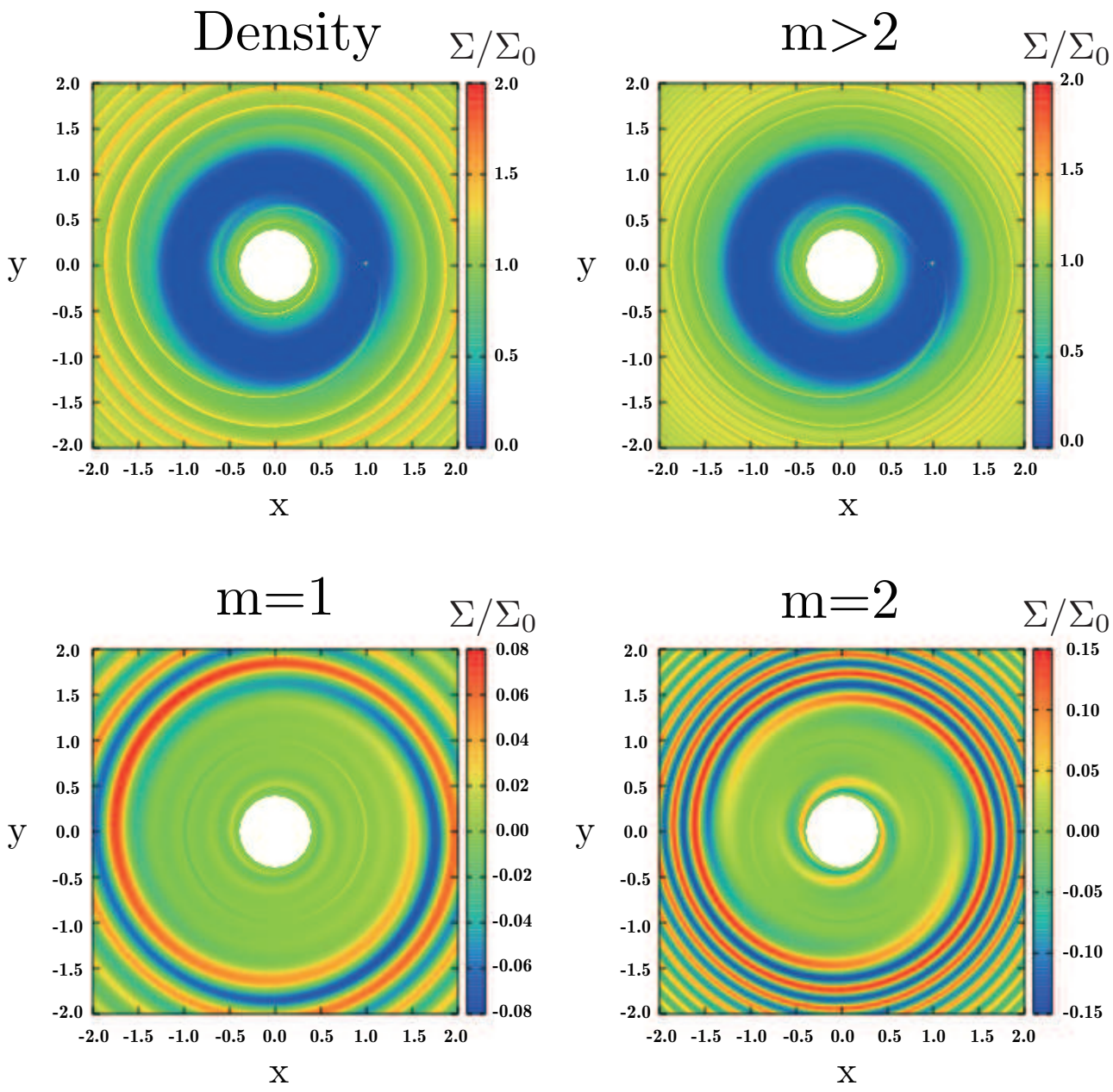

Figure 13. Two-dimensional surface density distribution in the case of $M_p/M_* = 10^{-3}$, $h/R_p = 1/20$, and $\alpha = 10^{-3}$. Shown are the surface densities produced by all modes (left top), the $m > 2$ modes (right top), the $m = 1$ mode (left bottom), and the $m = 2$ mode (right bottom).

gap structures obtained by the two-dimensional simulations. Our results can be summarized as follows:

(i) In order to reach the saturated full width, the viscous time defined by equation (9) is necessary. The gap depth reach the saturated value more rapidly; see Figures 1 and 2.

(ii) We derived a scaling relation for the gap width; this is proportional to the dimensionless parameter K' (equation 8) to the power of 1/4 when the gap width is measured by using the location of $\Sigma/\Sigma_0 = 0.1$–0.8, as in equation (12); see Figure 3. We also derived an empirical formula for the surface density distribution of the gap (equation 13), and this accurately reproduces the results of hydrodynamic simulations; see Figure 4.

(iii) Our model puts a constraint on the origin of the observed gap structure, as discussed in Section 3.4. Using equations (19) and (20), we can judge whether an observed gap is induced by the planet; see Figure 6.

(iv) We obtained an empirical model of equation (36) with the parameters x_d and w_d, which were obtained by equations (38) and (39). This model describes wave propagation that is consistent with the results of the hydrodynamic simulations; see Figure 9.

(v) Using the above model for the wave propagation, we constructed a semianalytical model of the gap structures. It accurately reproduces the radial surface density distributions given by the two-dimensional hydrodynamic simulations; see Figure 8.

We also discuss the dependence of the wave excitation and propagation on the planet mass; see Section 5. Our results show that the wave excitation and propagation are qualitatively different depending on the planet mass (Figure 11). In the case of a small planet ($M_{\rm p} \lesssim (h_{\rm p}/R_{\rm p})^3 M_*$), all the waves are excited and damping occurs only in the vicinity of the planet. On the other hand, in the case of a large planet ($M_{\rm p} > (h_{\rm p}/R_{\rm p})^3 M_*$), the waves are excited not only in the vicinity of the planet but also at distant locations. The damping of the waves slows down as the mass of the planet increases, and thus the planetary torque is deposited very far from the planet.

In the case of a large planet, the planetary torque exerted on the lower-order resonances is as significant as the torque exerted on the higher-order resonances (top panel of Figure 12; also see Appendix B). Because of the contributions from the lower-order resonances, the planetary torque increases even at locations far from the planet. The angular momentum is deposited by the waves with lower azimuthal numbers in the regions far from the planet (bottom panel of Figure 12). In particular, the contributions from the $m = 1$ and $m = 2$ components are significant. The contribution of the $m = 1$ mode is mainly due to the indirect term in the gravitational potential; this comes from the star–planet gravitational interaction. The contribution when $m = 2$ is due to the nonlinear interactions between the waves with a deep gap, as discussed in the recent literature (Juhász et al. 2015; Lee 2016).

Also, as discussed in the literature (e.g., Juhász et al. 2015; Fung & Dong 2015), a large planet excites the secondary wave, which is then launched from the site opposite from the planet; this is in addition to the primary wave, which is launched in the vicinity of the planet. The development of the contributions from the lower-order resonances is closely connected to the morphology of the secondary wave. As shown in Figure 13, the secondary wave is mainly composed of the contributions from the $m = 1$ and $m = 2$ components. Because of this, the secondary wave would be launched from a site that is almost opposite from the planet. For a planet of moderate mass, as shown by Fung & Dong (2015), the launching point of the secondary wave would move toward the planet, due to the effect of the contributions from the $m = 3$ and $m = 4$ components; in this case, this is the same level as for the $m = 1$ and $m = 2$ modes (see Appendix B).

The excitation and propagation of the waves is completely different in the cases of a large planet and a small planet. The wave excitation and propagation are quite important in determining the gap structure and morphology of the density wave, as summarized above. However, these theoretical mechanisms are not yet completely understood. To understand the mechanism of the gap formation and the morphology of the density waves induced by a giant planet, it will be necessary to further investigate the wave excitation and propagation when there are deep gaps.

ACKNOWLEDGEMENTS

This work was supported by JSPS KAKENHI Grant Numbers 23103004, 26103701, 26800106, and 26800229, and the Polish National Science Centre MAESTRO grant DEC-2012/06/A/ST9/00276. KDK was supported by the ALMA Japan Research Grant of the NAOJ Chile Observatory, NAOJ-ALMA-0135. Numerical computations were carried out on the Cray XC30 at the Center for Computational Astrophysics, National Astronomical Observatory of Japan and the Pan-Okhotsk Information System at the Institute of Low Temperature Science, Hokkaido University.

REFERENCES

ALMA Partnership et al., 2015, ApJ, 808, L3
Akiyama E., et al., 2015, ApJ, 802, L17
Akiyama E., et al., 2016, preprint, (arXiv:1607.04708)
Artymowicz P., Lubow S. H., 1992, ApJ, 389, 129
Artymowicz P., Lubow S. H., 1994, ApJ, 421, 651
Baruteau C., et al., 2014, Protostars and Planets VI, pp 667–689
Benisty M., et al., 2015, A&A, 578, L6
Burke C. J., et al., 2014, ApJS, 210, 19
Cameron A. G. W., 1978, Moon and Planets, 18, 5
Christiaens V., Casassus S., Perez S., van der Plas G., Ménard F., 2014, ApJ, 785, L12
Crida A., Morbidelli A., Masset F., 2006, Icarus, 181, 587
Currie T., Cloutier R., Brittain S., Grady C., Burrows A., Muto T., Kenyon S. J., Kuchner M. J., 2015, ApJ, 814, L27
Dipierro G., Price D., Laibe G., Hirsh K., Cerioli A., Lodato G., 2015, MNRAS, 453, L73
Dong R., Rafikov R. R., Stone J. M., 2011, ApJ, 741, 57
Duffell P. C., 2015, ApJ, 807, L11
Duffell P. C., Chiang E., 2015, ApJ, 812, 94
Duffell P. C., MacFadyen A. I., 2013, ApJ, 769, 41
Flock M., Ruge J. P., Dzyurkevich N., Henning T., Klahr H., Wolf S., 2015, A&A, 574, A68
Fung J., Chiang E., 2016, preprint, (arXiv:1606.02299)
Fung J., Dong R., 2015, ApJ, 815, L21
Fung J., Shi J.-M., Chiang E., 2014, ApJ, 782, 88
Goldreich P., Tremaine S., 1980, ApJ, 241, 425
Goodman J., Rafikov R. R., 2001, ApJ, 552, 793
Grady C. A., et al., 2013, ApJ, 762, 48
Ida S., Lin D. N. C., Nagasawa M., 2013, ApJ, 775, 42
Juhász A., Benisty M., Pohl A., Dullemond C. P., Dominik C., Paardekooper S.-J., 2015, MNRAS, 451, 1147
Kanagawa K. D., Fujimoto M. Y., 2013, ApJ, 765, 33
Kanagawa K. D., Tanaka H., Muto T., Tanigawa T., Takeuchi T., 2015a, MNRAS, 448, 994
Kanagawa K. D., Muto T., Tanaka H., Tanigawa T., Takeuchi T., Tsukagoshi T., Momose M., 2015b, ApJ, 806, L15
Kanagawa K. D., Muto T., Tanaka H., Tanigawa T., Takeuchi T., Tsukagoshi T., Momose M., 2016, PASJ, 68, 43
Kley W., 1999, MNRAS, 303, 696
Lee W.-K., 2016, preprint, (arXiv:1604.08941)
Lin D. N. C., Papaloizou J., 1979, MNRAS, 186, 799
Lynden-Bell D., Pringle J. E., 1974, MNRAS, 168, 603
Masset F., 2000, A&AS, 141, 165
Miyoshi K., Takeuchi T., Tanaka H., Ida S., 1999, ApJ, 516, 451
Mizuno H., 1980, Progress of Theoretical Physics, 64, 544
Momose M., et al., 2015, PASJ, 67, 83
Mordasini C., Alibert Y., Benz W., Klahr H., Henning T., 2012, A&A, 541, A97
Muto T., Inutsuka S.-i., 2009, ApJ, 701, 18
Muto T., Suzuki T. K., Inutsuka S.-i., 2010, ApJ, 724, 448
Muto T., et al., 2012, ApJ, 748, L22

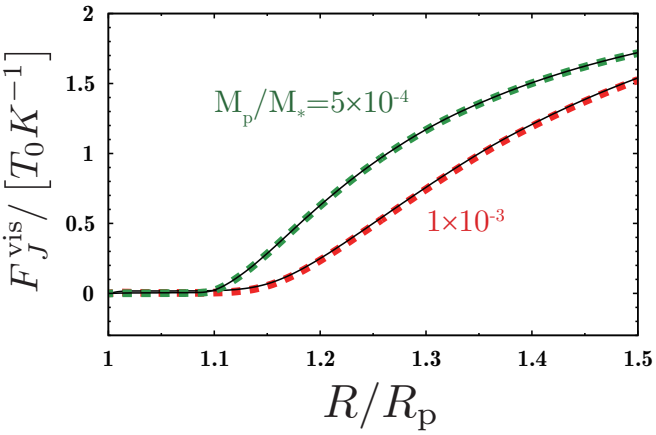

Figure A1. Distribution of the angular momentum flux due to the viscous diffusion for $M_{\rm p}/M_* = 5\times10^{-4}$ and 10^{-3}. The thick dashed lines are the azimuthally averaged flux obtained by equation (26), and the thin solid lines are the azimuthally averaged flux obtained by only the first term of equation (26).

Nomura H., et al., 2016, ApJ, 819, L7
Okuzumi S., Momose M., Sirono S.-i., Kobayashi H., Tanaka H., 2016, ApJ, 821, 82
Osorio M., et al., 2014, ApJ, 791, L36
Picogna G., Kley W., 2015, A&A, 584, A110
Rafikov R. R., 2002, ApJ, 569, 997
Rosotti G. P., Juhasz A., Booth R. A., Clarke C. J., 2016, MNRAS, 459, 2790
Sallum S., et al., 2015, Nature, 527, 342
Shakura N. I., Sunyaev R. A., 1973, A&A, 24, 337
Takahashi S. Z., Inutsuka S.-i., 2016, preprint, (arXiv:1604.05450)
Takeuchi T., Miyama S. M., 1998, PASJ, 50, 141
Takeuchi T., Miyama S. M., Lin D. N. C., 1996, ApJ, 460, 832
Tanaka H., Takeuchi T., Ward W. R., 2002, ApJ, 565, 1257
Tanigawa T., Watanabe S.-i., 2002, ApJ, 580, 506
Tsukagoshi T., et al., 2016, preprint, (arXiv:1605.00289)
Varnière P., Quillen A. C., Frank A., 2004, ApJ, 612, 1152
Ward W. R., 1986, Icarus, 67, 164
Ward W. R., 1997, Icarus, 126, 261
Yen H.-W., Liu H. B., Gu P.-G., Hirano N., Lee C.-F., Puspitaningrum E., Takakuwa S., 2016, ApJ, 820, L25
Zhang K., Blake G. A., Bergin E. A., 2015, ApJ, 806, L7
Zhu Z., Hartmann L., Nelson R. P., Gammie C. F., 2012a, ApJ, 746, 110
Zhu Z., Nelson R. P., Dong R., Espaillat C., Hartmann L., 2012b, ApJ, 755, 6
de Val-Borro M., et al., 2006, MNRAS, 370, 529
van der Marel N., van Dishoeck E. F., Bruderer S., Andrews S. M., Pontoppidan K. M., Herczeg G. J., van Kempen T., Miotello A., 2016, A&A, 585, A58

APPENDIX A: VISCOUS TRANSFER OF ANGULAR MOMENTUM

In the formulation of the semianalytical model described in Section 4, we assume that the second term of equation (26) is negligible compared to the first term. Figure A1 shows the viscous angular momentum flux obtained by using both terms in equation (26) and by using only the first term. As shown in the figure, the flux given by the first term is almost the same as the flux given by both terms.

APPENDIX B: DEPENDENCE OF THE WAVE EXCITATION AND PROPAGATION IN THE LOWER-M MODES ON THE PLANET MASS

Figure B1 shows the contributions from a smaller azimuthal number m on the planetary torque and the deposited torque for various values of the planet mass. As a comparison, we also plot the sum of the contributions from the components for which $m > 4$. When $M_{\rm p}/M_* = 10^{-4}$, the contributions from the components for which m is smaller are negligible compared with the contributions from the components for which m is larger; this is true for both the planetary torque and deposited torque. On the other hand, as the planet mass increases, the contributions from the components for which m is smaller become significant.

This paper has been typeset from a TEX/LATEX file prepared by the author.

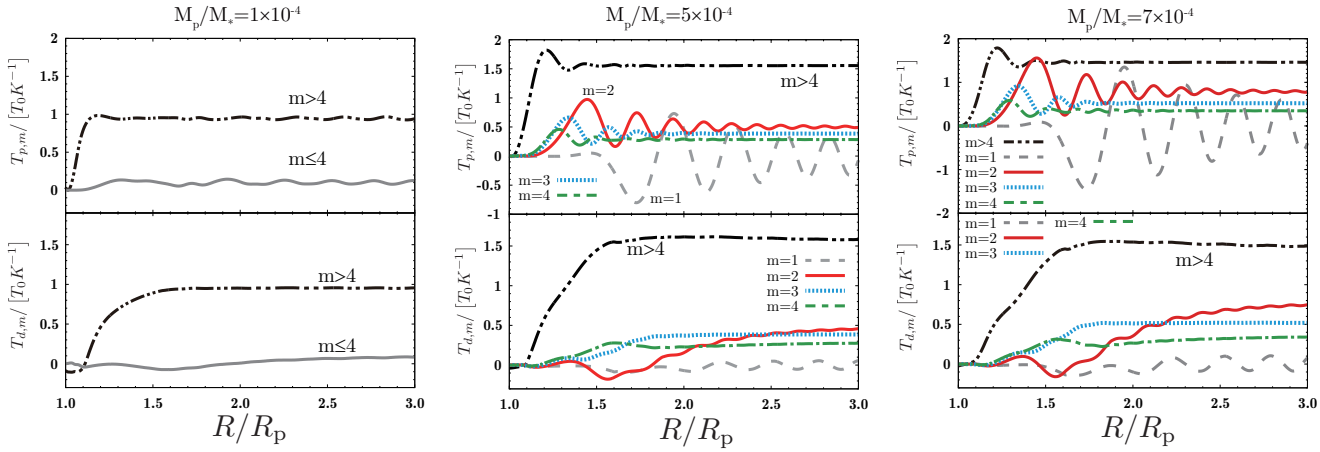

Figure B1. Same as Figure 12 but for $M_{\rm p}/M_* = 10^{-4}$(left), 5×10^{-4} (middle), and 7×10^{-4} (right). Note that because the contributions from the lower azimuthal wave numbers are very small when $M_{\rm p}/M_* = 10^{-4}$, we show only their sum (gray solid line).